Astronomy & Astrophysics manuscript no. output
March 17, 2025

Euclid Quick Data Release (Q1)

A first view of the star-forming main sequence in the Euclid Deep Fields

Euclid Collaboration: A. Enia[⋆,1,2], L. Pozzetti[2], M. Bolzonella[2], L. Bisigello[3], W. G. Hartley[4], C. Saulder[5,6], E. Daddi[7], M. Siudek[8,9], G. Zamorani[2], P. Cassata[10,3], F. Gentile[11,2], L. Wang[12,13], G. Rodighiero[10,3], V. Allevato[14], P. Corcho-Caballero[13], H. Domínguez Sánchez[15], C. Tortora[14], M. Baes[16], Abdurro'uf[17], A. Nersesian[18,16], L. Spinoglio[19], J. Schaye[20], Y. Ascasibar[21,22], D. Scott[23], E. Duran-Camacho[24,8], S. Quai[25,2], M. Talia[25,2], N. Aghanim[26], B. Altieri[27], A. Amara[28], S. Andreon[29], N. Auricchio[2], H. Aussel[7], C. Baccigalupi[30,31,32,33], M. Baldi[1,2,34], A. Balestra[3], S. Bardelli[2], A. Basset[35], P. Battaglia[2], R. Bender[5,6], A. Biviano[31,30], A. Bonchi[36], E. Branchini[37,38,29], M. Brescia[39,14], J. Brinchmann[40,41], S. Camera[42,43,44], G. Cañas-Herrera[45,46,20], V. Capobianco[44], C. Carbone[47], J. Carretero[48,49], S. Casas[50], F. J. Castander[9,51], M. Castellano[52], G. Castignani[2], S. Cavuoti[14,53], K. C. Chambers[54], A. Cimatti[55], C. Colodro-Conde[24], G. Congedo[56], C. J. Conselice[57], L. Conversi[58,27], Y. Copin[59], F. Courbin[60,61], H. M. Courtois[62], M. Cropper[63], A. Da Silva[64,65], H. Degaudenzi[4], G. De Lucia[31], A. M. Di Giorgio[19], C. Dolding[63], H. Dole[26], F. Dubath[4], C. A. J. Duncan[57], X. Dupac[27], S. Dusini[66], A. Ealet[59], S. Escoffier[67], M. Fabricius[5,6], M. Farina[19], R. Farinelli[2], F. Faustini[52,36], S. Ferriol[59], F. Finelli[2,68], S. Fotopoulou[69], M. Frailis[31], E. Franceschi[2], P. Franzetti[47], S. Galeotta[31], K. George[6], B. Gillis[56], C. Giocoli[2,34], P. Gómez-Alvarez[70,27], J. Gracia-Carpio[5], B. R. Granett[29], A. Grazian[3], F. Grupp[5,6], L. Guzzo[71,29,72], S. Gwyn[73], S. V. H. Haugan[74], J. Hoar[27], W. Holmes[75], I. M. Hook[76], F. Hormuth[77], A. Hornstrup[78,79], P. Hudelot[80], K. Jahnke[81], M. Jhabvala[82], B. Joachimi[83], E. Keihänen[84], S. Kermiche[67], A. Kiessling[75], B. Kubik[59], M. Kümmel[6], M. Kunz[85], H. Kurki-Suonio[86,87], Q. Le Boulc'h[88], A. M. C. Le Brun[89], D. Le Mignant[90], S. Ligori[44], P. B. Lilje[74], V. Lindholm[86,87], I. Lloro[91], G. Mainetti[88], D. Maino[71,47,72], E. Maiorano[2], O. Mansutti[31], O. Marggraf[92], M. Martinelli[52,93], N. Martinet[90], F. Marulli[25,2,34], R. Massey[94], D. C. Masters[95], S. Maurogordato[96], E. Medinaceli[2], S. Mei[97,98], M. Melchior[99], Y. Mellier[100,80], M. Meneghetti[2,34], E. Merlin[52], G. Meylan[101], A. Mora[102], M. Moresco[25,2], L. Moscardini[25,2,34], R. Nakajima[92], C. Neissner[103,49], S.-M. Niemi[45], J. W. Nightingale[104], C. Padilla[103], S. Paltani[4], F. Pasian[31], K. Pedersen[105], W. J. Percival[106,107,108], V. Pettorino[45], S. Pires[7], G. Polenta[36], M. Poncet[35], L. A. Popa[109], F. Raison[5], R. Rebolo[110,111,24], A. Renzi[10,66], J. Rhodes[75], G. Riccio[14], E. Romelli[31], M. Roncarelli[2], E. Rossetti[1], B. Rusholme[112], R. Saglia[6,5], Z. Sakr[113,114,115], A. G. Sánchez[5], D. Sapone[116], B. Sartoris[6,31], J. A. Schewtschenko[56], M. Schirmer[81], P. Schneider[92], T. Schrabback[117], M. Scodeggio[47], A. Secroun[67], G. Seidel[81], S. Serrano[51,118,9], P. Simon[92], C. Sirignano[10,66], G. Sirri[34], J. Skottfelt[119], L. Stanco[66], J. Steinwagner[5], C. Surace[90], P. Tallada-Crespí[48,49], A. N. Taylor[56], H. I. Teplitz[95], I. Tereno[64,120], S. Toft[121,122], R. Toledo-Moreo[123], F. Torradeflot[49,48], I. Tutusaus[114], L. Valenziano[2,68], J. Valiviita[86,87], T. Vassallo[6,31], G. Verdoes Kleijn[13], A. Veropalumbo[29,38,37], Y. Wang[95], J. Weller[6,5], A. Zacchei[31,30], F. M. Zerbi[29], I. A. Zinchenko[6], E. Zucca[2], M. Ballardini[124,125,2], E. Bozzo[4], C. Burigana[126,68], R. Cabanac[114], A. Cappi[2,96], D. Di Ferdinando[34], J. A. Escartin Vigo[5], L. Gabarra[127], M. Huertas-Company[24,8,128,129], J. Martín-Fleitas[102], S. Matthew[56], N. Mauri[55,34], R. B. Metcalf[25,2], A. Pezzotta[5], M. Pöntinen[86], C. Porciani[92], I. Risso[130], V. Scottez[100,131], M. Sereno[2,34], M. Tenti[34], M. Viel[30,31,33,32,132], M. Wiesmann[74], Y. Akrami[133,134], I. T. Andika[135,136], S. Anselmi[66,10,137], M. Archidiacono[71,72], F. Atrio-Barandela[138], C. Benoist[96], K. Benson[63], P. Bergamini[71,2], D. Bertacca[10,3,66], M. Bethermin[139], A. Blanchard[114], L. Blot[140,137], H. Böhringer[5,141,142], S. Borgani[143,30,31,32,132], A. S. Borlaff[144,145], M. L. Brown[57], S. Bruton[146], A. Calabro[52], B. Camacho Quevedo[51,9], F. Caro[52], C. S. Carvalho[120], T. Castro[31,32,30,132], F. Cogato[25,2], T. Contini[114], A. R. Cooray[147], O. Cucciati[2], S. Davini[38], F. De Paolis[148,149,150], G. Desprez[13], A. Díaz-Sánchez[151], J. J. Diaz[24], S. Di Domizio[37,38], J. M. Diego[15], P.-A. Duc[139], Y. Fang[6], A. G. Ferrari[34], P. G. Ferreira[127], A. Finoguenov[86], A. Fontana[52], F. Fontanot[31,30], A. Franco[149,148,150], K. Ganga[97], J. García-Bellido[133], T. Gasparetto[31], V. Gautard[11], E. Gaztanaga[9,51,152], F. Giacomini[34], F. Gianotti[2], G. Gozaliasl[153,86], M. Guidi[1,2], C. M. Gutierrez[154], A. Hall[56], S. Hemmati[112], C. Hernández-Monteagudo[111,24], H. Hildebrandt[155], J. Hjorth[105], J. J. E. Kajava[156,157], Y. Kang[4], V. Kansal[158,159], D. Karagiannis[124,160], K. Kiiveri[84], C. C. Kirkpatrick[84], S. Kruk[27], J. Le Graet[67], L. Legrand[161,162], M. Lembo[124,125], F. Lepori[163], G. Leroy[164,94], G. F. Lesci[25,2], J. Lesgourgues[50], L. Leuzzi[25,2], T. I. Liaudat[165], A. Loureiro[166,167], J. Macias-Perez[168], G. Maggio[31], M. Magliocchetti[19], E. A. Magnier[54], C. Mancini[47], F. Mannucci[169], R. Maoli[170,52], C. J. A. P. Martins[171,40], L. Maurin[26], M. Miluzio[27,172], P. Monaco[143,31,32,30], C. Moretti[33,132,31,30,32], G. Morgante[2], C. Murray[97], K. Naidoo[152], A. Navarro-Alsina[92],

S. Nesseris[133], F. Passalacqua[10,66], K. Paterson[81], L. Patrizii[34], A. Pisani[67,173], D. Potter[163], M. Radovich[3], P.-F. Rocci[26], S. Sacquegna[148,149,150], M. Sahlén[174], D. B. Sanders[54], E. Sarpa[33,132,32], C. Scarlata[175], A. Schneider[163], M. Schultheis[96], D. Sciotti[52,93], E. Sellentin[176,20], F. Shankar[177], L. C. Smith[178], S. A. Stanford[179], K. Tanidis[127], G. Testera[38], R. Teyssier[173], S. Tosi[37,130], A. Troja[10,66], M. Tucci[4], C. Valieri[34], A. Venhola[180], D. Vergani[2], G. Verza[181], P. Vielzeuf[67], N. A. Walton[178], and E. Soubrie[26]

(Affiliations can be found after the references)

March 17, 2025

ABSTRACT

The star-forming main sequence (SFMS) is a tight relation observed between stellar masses and star-formation rates (SFR) in a population of galaxies. The relation holds for different redshift, morphological, and environmental domains, and is a key to understanding the underlying relations between a galaxy budget of cold gas and its stellar content. *Euclid* Quick Data Release 1 (Q1) gives the opportunity to investigate this fundamental relation in galaxy formation and evolution. We complement the *Euclid* release with public IRAC observations of the *Euclid* Deep Fields (EDFs), improving the quality of recovered photometric redshifts, stellar masses, and star-formation rates, as shown both from simulations and comparison with available spectroscopic redshifts. From Q1 data alone, we recover more than ~ 30 k galaxies with $\log_{10}(M_*/M_\odot) > 11$, giving a precise constraint of the SFMS at the high-mass end. We investigated SFMS, in a redshift interval between 0.2 and 3.0, comparing our results with the existing literature and fitting them with a parameterisation taking into account the presence of a bending of the relation at the high-mass end, depending on the bending mass M_0. We find good agreement with previous results in terms of M_0 values. We also investigate the distribution of physical (e.g., dust absorption A_V and formation age) and morphological properties (e.g., Sérsic index and radius) in the SFR–stellar mass plane, and their relation with the SFMS. These results highlight the potential of *Euclid* in studying the fundamental scaling relations that regulate galaxy formation and evolution in anticipation of the forthcoming Data Release 1.

Key words. Galaxies: evolution; Galaxies: formation; Galaxies: fundamental parameters; Galaxies: statistics

1. Introduction

The star-forming main-sequence (SFMS) is a relation between stellar masses (M_*) and star-formation rates (SFRs) that is observed for star-forming galaxies (SFGs). It has been extensively studied in the last decades (Brinchmann et al. 2004; Daddi et al. 2007; Elbaz et al. 2011), investigating its slope, normalisation, scatter, and evolution over time (see Speagle et al. 2014; Popesso et al. 2023, and references therein). The SFMS is observed across different redshifts and is already in place by $z \sim 6$ (e.g., Cole et al. 2023; Clarke et al. 2024). It hosts the majority of star-formation at each epoch (Rodighiero et al. 2011), suggesting that galaxies spend most of their lifetime on the SFMS, undergoing secular evolution. The tightness of the relation, with a typical scatter of 0.3 dex, implies its universality as the main mode of galaxy growth.

This relation emerges from the interplay between the stellar content of galaxies and their cold gas reservoirs (i.e., the so-called Kennicutt–Schmidt relation from Schmidt 1959 and Kennicutt 1998b, and the resolved molecular gas main-sequence, see e.g. Lin et al. 2019; Morselli et al. 2020; Ellison et al. 2021), and it has been shown to hold also at sub-kpc scales (e.g., Wuyts et al. 2013; Hsieh et al. 2017; Lin et al. 2017; Abdurro'uf & Akiyama 2017; Ellison et al. 2018; Enia et al. 2020; Baker et al. 2022).

At masses $\log_{10}(M_*/M_\odot) > 10$ at $0 < z < 1$ and at the high-mass end $\log_{10}(M_*/M_\odot) > 11$ at $z \sim 2$, the relation appears to exhibit a deviation from the linear trend, the so-called *bending* of the SFMS (Whitaker et al. 2014; Schreiber et al. 2015; Tomczak et al. 2016; Popesso et al. 2019; Leja et al. 2022; Daddi et al. 2022a; Leroy et al. 2024; Wang et al. 2024). The bending traces changes in cold-gas accretion (Kereš et al. 2005; Dekel & Birnboim 2006) and availability for star-formation processes, and could be a consequence of the reduced availability of cold gas in halos entering the hot-accretion mode phase (Daddi et al. 2022a), or feedback from active galactic nuclei (Fabian 2012), or both (Bower et al. 2017). Additionally, the reactivation of star formation in the disks of galaxies that are approaching quiescence or have already been quenched may also contribute to the bending of the SFMS (Mancini et al. 2019). This turnover mass can be linked with the host halo mass quenching threshold (Yang et al. 2007; Behroozi et al. 2019; Popesso et al. 2023), defining the transition between an environment favourable to star-formation to a regime where these processes are suppressed.

The Euclid Quick Release Q1 (2025) is the first release of *Euclid* survey data, corresponding to a single Reference Observing Sequence (ROS, see Euclid Collaboration: Scaramella et al. 2022) of the Euclid Deep Fields (EDFs). This is a homogeneous view of a large area of the extragalactic sky ($\sim 63\,\mathrm{deg}^2$) from optical to near-infrared (NIR), complemented with observations of the same fields at 3.6 µm and 4.5 µm with the Infrared Array Camera (IRAC, Fazio et al. 2004) on *Spitzer* (Werner et al. 2004). These fields have the potential to become the most well-studied extragalactic fields of the coming decades. In this work, we illustrate the results obtained with the data and products of Q1 for the SFMS, investigating its evolution up to $z = 3$, and the distribution of physical and morphological parameters along the SFMS, as well as validating these results with the existing literature, a first demonstration of the potential of *Euclid* to investigate scaling relations and the baryon cycle.

This paper is structured as follows. In Sect. 2, we describe the data released for Q1. In Sect. 3, we describe the methods used to recover the photometric redshifts and physical parameters (PPs). In the same Sect., we validate the results, reporting the performance of our methods on simulations and the available subsample of spectroscopic redshifts and Hα-estimated star-formation rates. In Sect. 4, we report the results for the SFMS. In Sect. 5, we present our conclusions and perspectives for the upcoming Data Release 1.

Throughout this paper we adopt a flat Lambda cold dark matter (ΛCDM) cosmology with $H_0 = 70\,\mathrm{km\,s^{-1}\,Mpc^{-1}}$, $\Omega_\mathrm{m} = 0.3$, and $\Omega_\Lambda = 0.7$, and assume a Chabrier (2003) initial mass function (IMF). All magnitudes are given in the AB photometric system (Oke & Gunn 1983).

⋆ e-mail: andrea.enia@unibo.it

Table 1. Filters used in this work, with associated observed depths.

Band	$\lambda_{\rm eff}$ [µm]	EDF-N	EDF-F	EDF-S
$u_{\rm CFHT/MegaCam}$	0.372	23.39		
$g_{\rm HSC}$	0.480	24.87		
$r_{\rm CFHT/MegaCam}$	0.640	24.01		
$i_{\rm PAN-STARRS}$	0.755	23.07		
$z_{\rm HSC}$	0.891	23.35		
$g_{\rm Decam}$	0.473		24.65	24.72
$r_{\rm Decam}$	0.642		24.33	24.37
$i_{\rm Decam}$	0.784		23.76	23.78
$z_{\rm Decam}$	0.926		23.06	23.12
VIS/$I_{\rm E}$	0.715	24.75	24.70	24.74
NISP/$Y_{\rm E}$	1.085	23.16	23.10	23.15
NISP/$J_{\rm E}$	1.375	23.31	23.24	23.30
NISP/$H_{\rm E}$	1.773	23.24	23.19	23.24
IRAC1	3.550	24.05	24.05	23.15
IRAC2	4.493	23.95	23.95	23.05

Notes. Reported magnitudes are the 10σ observed median depths of the observing tiles for an extended source in a 2×FWHM diameter aperture. For IRAC values see Euclid Collaboration: Moneti et al. (2022) and Euclid Collaboration: McPartland et al. (2024).

2. Data

A detailed description of the Q1 data release is presented in Euclid Collaboration: Aussel et al. (2025), Euclid Collaboration: McCracken et al. (2025), Euclid Collaboration: Polenta et al. (2025), and Euclid Collaboration: Romelli et al. (2025). A summary of the scientific objectives of the mission can be found in Euclid Collaboration: Mellier et al. (2024). In short, for Q1 *Euclid* observed $\sim 63\,\mathrm{deg}^2$ of the extragalactic sky, divided in the EDF-North (EDF-N), EDF-Fornax (EDF-F), and EDF-South (EDF-S), in four photometric bands, one in the visible ($I_{\rm E}$, Euclid Collaboration: Cropper et al. 2024), and three in the NIR ($Y_{\rm E}$, $J_{\rm E}$, and $H_{\rm E}$, Euclid Collaboration: Jahnke et al. 2024). These observations are complemented by ground-based observations carried out with multiple instruments to cover the wavelength range between 0.3 µm and 1.8 µm by the Ultraviolet Near-Infrared Optical Northern Survey (UNIONS, Gwyn et al. in prep) and the Dark Energy Survey (DES, Flaugher et al. 2015; Dark Energy Survey Collaboration et al. 2016).

In order to obtain robust results and improve the quality of the recovered photometric redshifts and PPs (see Sect. 3.3) we also added to the *Euclid* photometry two available IRAC bands, at 3.6 µm and 4.5 µm, covering all the EDFs (Euclid Collaboration: Moneti et al. 2022; Euclid Collaboration: McPartland et al. 2024). More details on how IRAC photometry is measured can be found in Euclid Collaboration: Bisigello et al. (2025).

In Table 1 we report the filters used in this work, with the observed 10σ depths for an extended source in an aperture that is twice the full width at half maximum (FWHM, i.e., the worst one among the optical and *Euclid* bands, see Euclid Collaboration: Romelli et al. 2025, for further details). For this work, we start from the available *Euclid* catalogues and apply a series of selections to make our analysis more robust, removing compact or low-quality sources. These selections are:

- SPURIOUS_FLAG = 0;
- DET_QUALITY_FLAG < 4;
- MUMAX_MINUS_MAG > −2.6.

For further details on the meaning of the flags, see Euclid Collaboration: Tucci et al. (2025). This selection skims the sample from stars and compact objects such as quasi-stellar objects (QSOs).

We further clean our sample from these two classes of objects using the classification probability of the Q1 data products, imposing the following criteria:

- PROB_QSO < 0.86;
- PROB_STAR < 0.10.

See Sect. 4 of Euclid Collaboration: Tucci et al. (2025) for further details, and also Euclid Collaboration: Matamoro Zatarain et al. (2025) about the classification thresholds.

Finally, we benefit from the results of the morphological analysis for Q1 (Euclid Collaboration: Walmsley et al. 2025; Euclid Collaboration: Quilley et al. 2025), applying another set of cuts related to the morphological parameters and the size of the source. We keep sources with:

- $q > 0.05$;
- $0.01a < R_{\rm e} < 2a$.

q is the Sérsic axis ratio, $R_{\rm e}$ the Sérsic radius, and a the isophote semi-major axis, in units of VIS pixels. For further information see Sect. 4 and the left panel of Fig. 3 in Euclid Collaboration: Quilley et al. (2025). These further remove diffraction spikes, cosmic rays, or stars that survived the cuts described above.

The last cut that we apply is in magnitude, in order to work with a mass-complete sample, limiting our analysis to sources with observed $H_{\rm E} < 24$, corresponding to an average measured signal-to-noise ratio of five, measured from the $2 \times$ FWHM aperture photometry. Our final sample is composed of 8 090 074 sources.

3. Physical properties and validation

We refer the reader to Euclid Collaboration: Tucci et al. (2025) for a complete and exhaustive description of how the Q1 data have been processed to infer photometric redshifts and PPs. In this Section, we briefly summarise the procedure.

Due to the large number of sources detected (of the order of tens of millions) in the EDFs, machine learning (ML) methods have been developed to speed up the computational process while achieving a comparable performance of template fitting methods (see e.g., Euclid Collaboration: Desprez et al. 2020; Euclid Collaboration: Enia et al. 2024). Data products produced for Q1 have been obtained with a nearest-neighbours (NNs) algorithm, `nnpz`, which finds a k–number of NNs (30 in the *Euclid* pipeline, 80 for this work) in the template space (i.e., magnitude and colour) for each target galaxy from a reference sample, and infers the photometric redshifts and PPs from those.

The reference sample differs from the one used to produce the Q1 data products, the reason for which will be clear in a few paragraphs. It has been built from a grid of templates (Bruzual & Charlot 2003, in the 2016 version[1]), using the MILES stellar library, which adopts the Kroupa (2001) IMF, which we therefore converted to Chabrier (2003) for PPs. The models have been built with exponentially delayed star-formation histories:

$$\mathrm{SFR}(t) \propto (t - T_0)\, \mathrm{e}^{-(t-T_0/\tau)}, \qquad (1)$$

drawn from a Halton (1964) grid[2] in a 6-dimensional space with the following free parameters:

- redshifts: $0 < z < 7$;

[1] http://www.bruzual.org/bc03/Updated_version_2016/

[2] A method to generate a quasi-random grid, which is evenly distributed across the parameter space, minimising the presence of gaps and clusters of points.

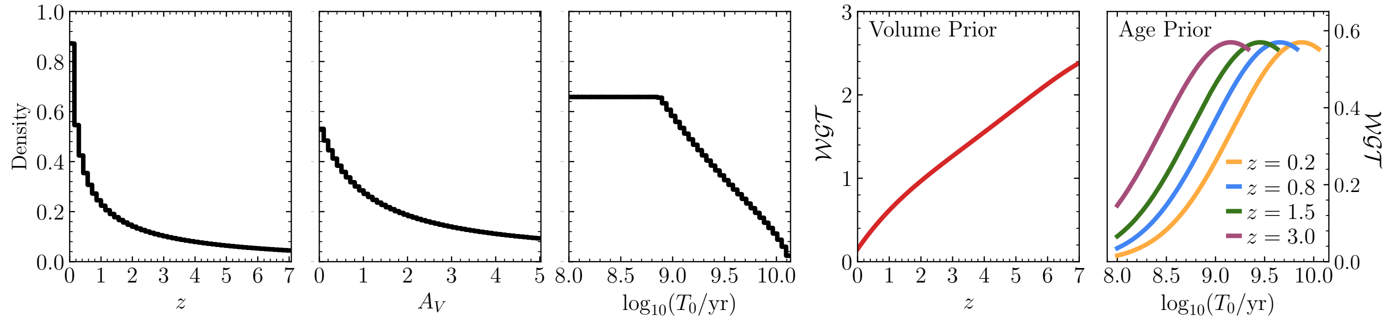

Fig. 1. *Left panels*: distribution of redshifts z, attenuations A_v, and ages T_0 for the reference sample used in this work. *Right panels*: the two priors adopted in this work – volume and age – as multiplicative weights on the reference galaxies, depending on their redshifts or ages.

– ages: $8 < \log_{10}(T_0/\mathrm{yr}) < 10.138$;
– e-folding timescale: $8 < \log_{10}(\tau/\mathrm{yr}) < 10.5$;
– ionisation parameter: $-4 < \log_{10}(U) < -2$;
– metallicities: $0.1 < Z/Z_{\odot} < 2$.

For dust attenuation, we generate models with both Calzetti et al. (2000) and SMC (Prevot et al. 1984) laws, with V-band attenuation A_V between 0 and 5. Stellar masses and SFRs are inferred from the amplitude of the observed spectral energy distribution (SED), as a scaling parameter recovered by nnpz. Metallicities and ionisation parameters are distributed uniformly within the given ranges; the same for τ, but on a logarithmic scale. The redshifts are distributed with a linear scaling in $(1 + z)$ steps, while ages and A_V scale logarithmically from the lowest value to the highest. For these last three parameters, their distribution in the reference sample is shown in black in the first three panels of Fig. 1. We then generate the noise-free observed-frame photometry associated with each model. In the end, the reference sample consists of 1 490 150 objects.

nnpz then finds the 80 NNs for every target galaxy, based on the observed magnitudes and colours. Each of these NNs will have its own weight – measured from the χ^2 distance between the reference and the target – and scaling parameter from the SED amplitude. By combining them, we measure the median (or the mode) of the distribution of NNs, which ultimately are the inferred photo-zs, PPs, and absolute magnitudes of the target galaxies.

Differently from what has been done in the *Euclid* pipeline, we add two more photometric points to the reference sample, accounting for the IRAC1 and IRAC2 channels (see Sect. 2). Moreover, having access to the nnpz results – that is, the set of NNs for each target galaxy – we can impose whatever physically motivated condition (i.e., a prior) directly on the NNs, either by measuring the output z_{phot} or PPs only on the set of NNs that satisfy the condition, or by re-weighting differently the NNs in the reference sample in order to penalise unphysical solutions.

As reported in Sect. 6.1.1 of Euclid Collaboration: Tucci et al. (2025), the Q1 pipeline results (obtained without the application of any condition to the NNs) contain an artificially high number of low-z galaxies with extremely young ages – $\log_{10}(T_0/\mathrm{yr})$ starts from 7 in the pipeline – observed at the peak of their star-forming activity, thus at the limit of specific star-formation rate (sSFR) inherent to parametric models ($\log_{10}\mathrm{sSFR/yr^{-1}} \simeq -7.8$, see Fig. 8 of Ciesla et al. 2017). The resulting redshift distribution is ultimately skewed towards non-physically high number counts at low-z, creating an artefact straight line at the sSFR saturation limit in the SFMS plot (see Fig. 14 in Euclid Collaboration: Tucci et al. 2025). In principle, this issue could be addressed in the Q1 pipeline data product by imposing an age prior on the NNs, for example, ignoring those with ages < 0.1 Gyr. This would significantly reduce the impact of artefacts, but at the cost of reducing the Q1 sample by about 40%, excluding from the sample all sources without even a single NN that satisfies the prior. Losing these sources would introduce systematic biases in our analysis. To avoid this, we take some precautions that deviate from what has been done in the pipeline, in order to reduce the impact of those artefact sources without losing a significant fraction of the sample: the boundaries for ages and A_{V} mentioned above used to generate the reference sample for this work are different from those reported in Euclid Collaboration: Tucci et al. (2025), with $0 < A_{\mathrm{V}} < 3$ and $7 < \log_{10}(T_0/\mathrm{yr}) < 10.138$. We also increase the k–number of NNs to 80. Finally, we impose both a volume and an age prior to the NNs in the reference sample.

With the volume prior, we increase the weights of NNs at higher redshifts compared to those at lower redshifts, where the volume of the Universe sampled by the survey is smaller and fewer galaxies are expected to be observed. This prior is implemented as a multiplicative weight assigned to each object in the reference sample, and only depends on the redshift as

$$\mathcal{WGT}(z) \propto \frac{\mathrm{d}V_{\mathrm{c}}(z)}{\mathrm{d}z}, \qquad (2)$$

where $\mathrm{d}V_{\mathrm{c}}(z)$ is the comoving volume shell in the interval $[z, z + \mathrm{d}z]$. This prior is shown in red in the centre-right panel of Fig. 1.

The age prior is once again a multiplicative weight $\mathcal{WGT}(T_0)$ to apply on NNs. This takes into account the fact that younger galaxies could be observed at higher redshifts, while this possibility should be reduced at low redshifts. In building the prior, we check the distribution of ages in different redshift bins in the 2 deg^2 of the Cosmic Evolution Survey (COSMOS, Weaver et al. 2022), finding that these can be modelled as normal distributions with peak age decreasing while moving at higher redshift. This weight is then constructed as a truncated normal distribution centred at two-thirds the age of the Universe at any given z, with width 0.7 in $\log_{10}(T_0/\mathrm{yr})$. A weight equal to zero is assigned for those sources with an age greater than the age of the Universe at the given z. The shape of the age prior is reported in the rightmost panel of Fig. 1 for four indicative redshift values.

This procedure makes us sensitive to the bulk of the population of SFGs, while reducing our ability to properly identify and describe outliers (e.g., the starburst galaxies, as the presence of a star-forming burst is not directly accounted for in the reference sample). Given the main scopes of this work, this is acceptable, since it has been found that the exponentially delayed τ model is an accurate description of the star-formation histories of the main population of SFMS galaxies, at least at $z < 2$ (see

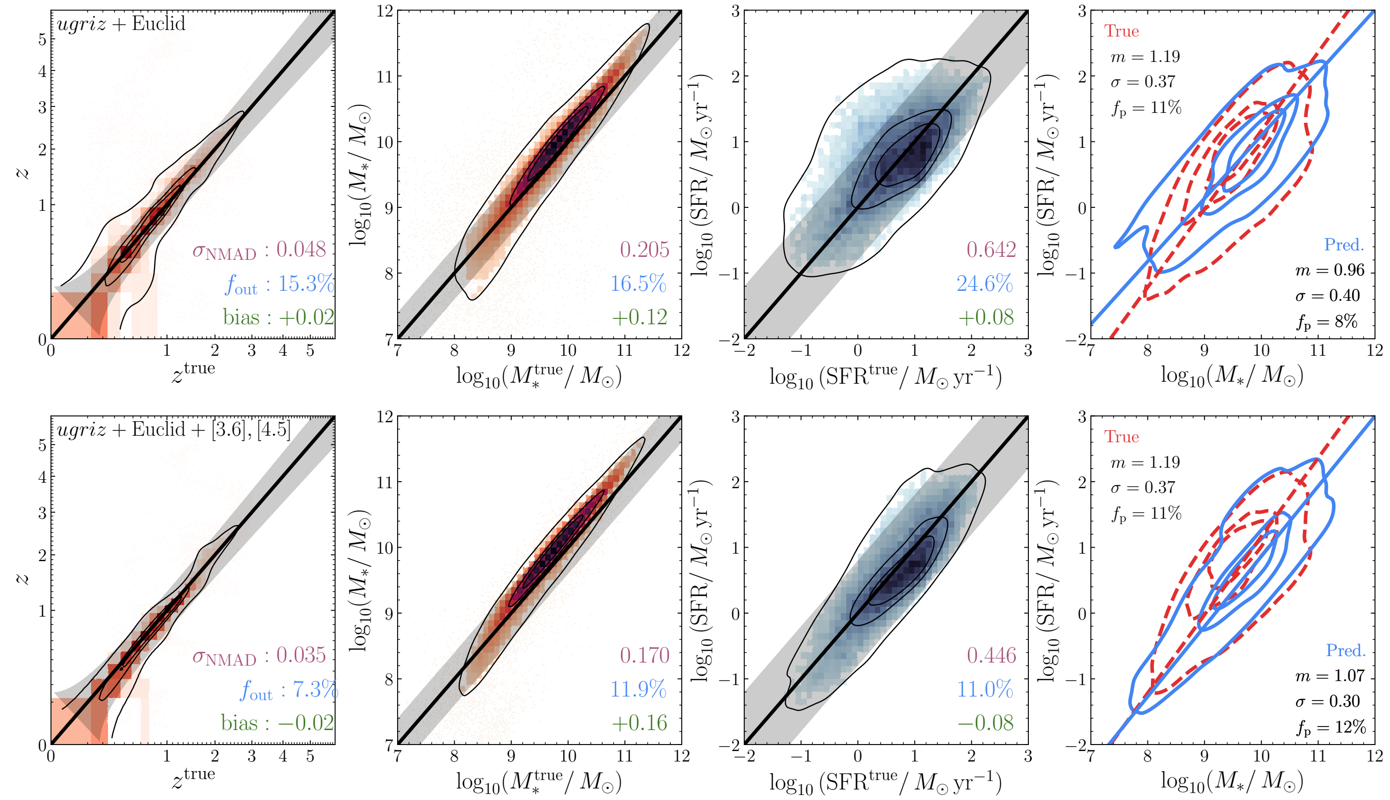

Fig. 2. Results for the `nnpz` run on the FS2 galaxies, without (*top panels*) and with the first two WISE filters (*bottom panels*). The black line is the 1:1 relation; the shaded area is the region beyond which a prediction is an outlier. In every plot, the contours are the area containing 86%, 39% (corresponding to the 2σ and 1σ levels for a 2D histogram) and 20% of the sample. For SFMS (right panel) the true distribution is reported in red (dashed), the predicted one in blue (solid). The lines are the orthogonal distance regression (ODR) best-fit to the distribution with passive galaxies removed. The reported metrics are NMAD (purple), the outlier fraction $f_{\rm out}$ (blue), and the bias (green) for the photometric redshifts and physical parameters, and the slope m, scatter σ, and fraction of passive galaxies $f_{\rm p}$ for the SFMS, all defined in Sect. 3.1.

e.g., Speagle et al. 2014; Ciesla et al. 2017). Recently, studies focussing on non-parametric models of star-formation histories have found how these models could better recover the complex events that arise during the evolution of a galaxy (Iyer et al. 2019; Leja et al. 2019; Baes et al. 2020).

In the future, for Data Release 1, models will better account for starburst galaxies, with the possibility of exploring other regions of the parameter space, even accounting for complex star-formation histories (see for example Euclid Collaboration: Corcho-Caballero et al. 2025).

We validate our results both on the available state-of-the-art simulations adapted to reproduce as closely as possible *Euclid* observations (i.e., the Flagship2 simulation, FS2, see Euclid Collaboration: Castander et al. 2024), and on a compilation of the available spectroscopic redshifts and Hα measured SFRs in the EDFs. Although the latter is fundamental to assess the quality of recovered photometric redshifts with what can be interpreted as the closest possible thing to a "ground truth" value, the former is unavoidable to put a degree of confidence in other recovered quantities such as stellar masses and SFRs.

3.1. Metrics for quality assessment

The metrics used to quantify the quality of the results are defined differently when referring to redshifts or PPs. We refer the reader to Euclid Collaboration: Enia et al. (2024) for a full discussion of thresholds and catastrophic outlier definitions; here, we simply report the definitions.

We first define a set of true values $z_{\rm test}$ and $y_{\rm test}$ (on a logarithmic scale for PPs), to confront with the predicted values $z_{\rm pred}$ and $y_{\rm pred}$. We then define the normalised median absolute deviation as

$$\mathrm{NMAD} = 1.48 \times \mathrm{median}\begin{cases} \dfrac{|z_{\rm pred} - z_{\rm test}|}{1 + z_{\rm test}} - b, & \text{for redshifts,} \\ |y_{\rm pred} - y_{\rm test}| - b, & \text{for PPs,} \end{cases} \quad (3)$$

with b being the model bias (see below).

Then the outlier fraction

$$f_{\rm out} = \begin{cases} \dfrac{|z_{\rm pred} - z_{\rm test}|}{1 + z_{\rm test}} > 0.15, & \text{for redshifts,} \\ |y_{\rm pred} - y_{\rm test}| > t_{\rm out}, & \text{for PPs,} \end{cases} \quad (4)$$

with $t_{\rm out} = 0.4$ for stellar masses and $t_{\rm out} = 0.8$ for SFRs.

Finally, the bias,

$$b = \mathrm{median}\begin{cases} \left(\dfrac{z_{\rm pred} - z_{\rm test}}{1 + z_{\rm test}}\right), & \text{for redshifts,} \\ (y_{\rm pred} - y_{\rm test}), & \text{for PPs.} \end{cases} \quad (5)$$

3.2. Validation on simulations

We randomly select about 70 k sources from a complete octant of the FS2 simulation (Euclid Collaboration: Castander et al. 2024). We checked that the selection does not skew the ground-truth values with respect to the full distribution. These mock

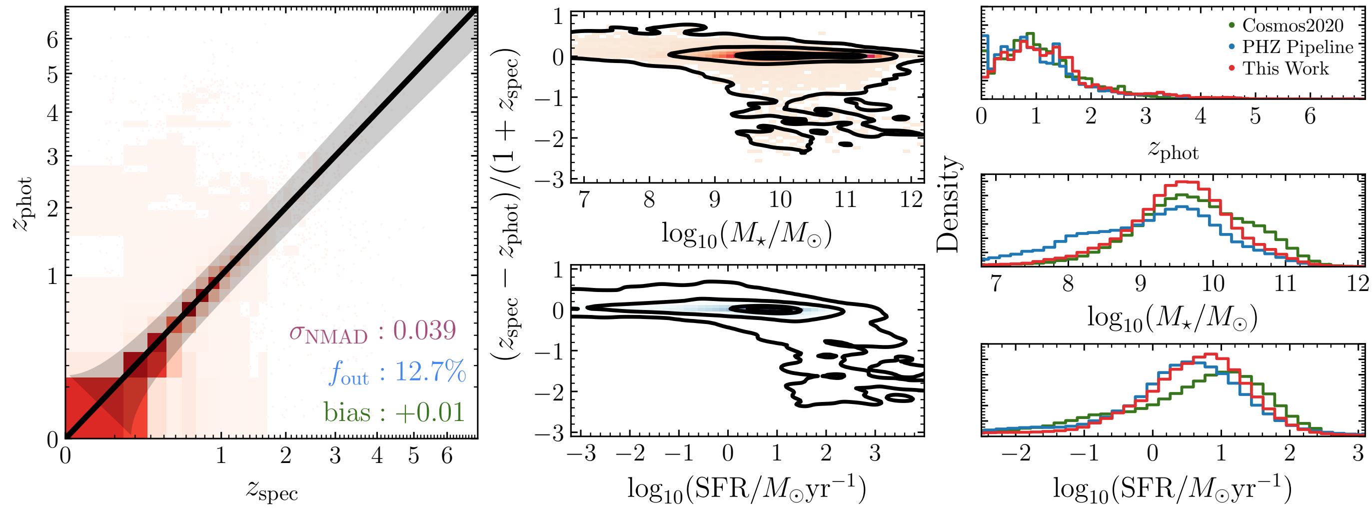

Fig. 3. *Left*: comparison between the measured photometric redshifts and a compilation of all the available and reliable spectroscopic redshifts, colour-coded by the density of objects in each bin. The black line is the 1:1 relation, while the shaded area is the region beyond which a prediction is considered to be an outlier. The reported metrics are NMAD (purple), the outlier fraction $f_{\rm out}$ (blue) and the bias (green), all defined in Sect. 3.1. *Middle*: normalised redshift difference as a function of stellar masses (top) and SFRs (bottom). The black contours are at the same levels as in Fig. 2. *Right*: normalised distributions of photometric redshifts (top), stellar masses (centre), and SFRs (bottom) for the our full sample (red), compared with the results coming from the Q1 data products (PHZ, in blue), and COSMOS2020 (green), at the same magnitude cuts applied in this work (see Sect. 2).

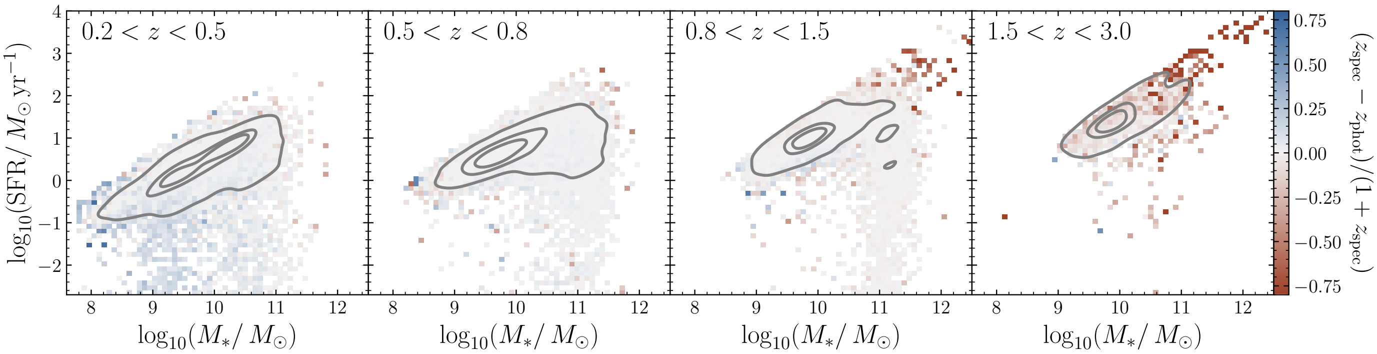

Fig. 4. The M_*–SFR plane in four different redshift intervals, only for the sources with a reliable $z_{\rm spec}$ described in Sect. 3.3, colour-coded by the median normalized redshift difference in each bin. To give an idea of the density of objects in each redshift interval, we superimpose the contours in gray, with the same levels as in Fig. 2.

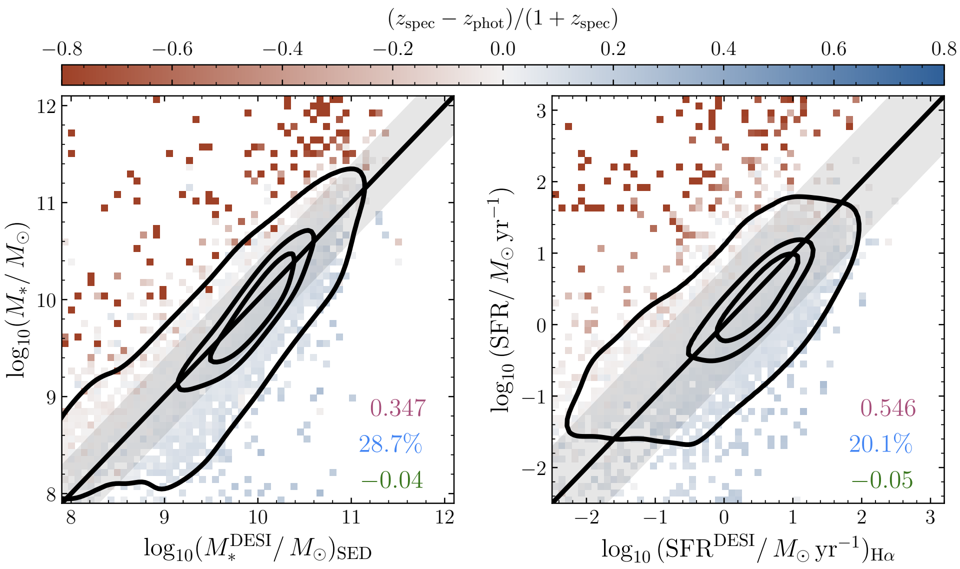

Fig. 5. Comparison between the stellar masses and SFRs measured in this work with a sample of objects from DESI with stellar masses from SED fitting (*left*) and SFRs from Hα (*right*), colour-coded as a function of the median normalised redshift difference in each bin. The black line is the 1:1 relation, while the shaded area is the region beyond which a prediction is an outlier. The contours are the same as in Fig. 2. The reported metrics are defined in Sect. 3.1.

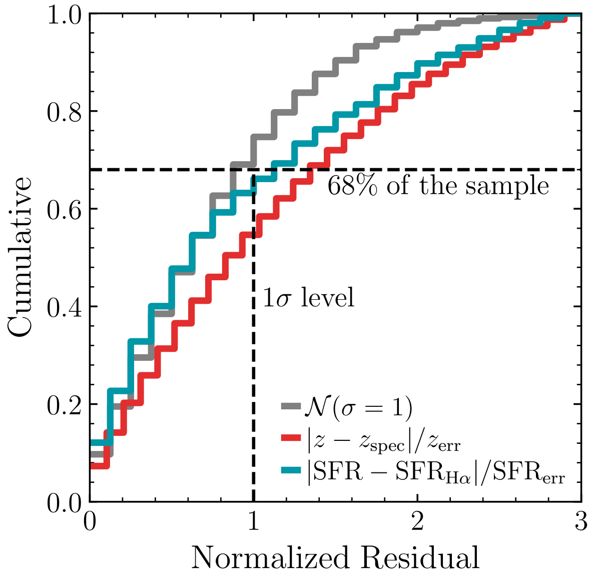

Fig. 6. Cumulative distribution of the normalized residuals for photometric redshifts (red) and SFRs (blue). For comparison, we also show in gray the cumulative of a normal distribution with $\sigma = 1$. Dashed black lines highlight the position where 68% of the distributions is, and the 1σ level for the residuals.

sources are, by construction, distributed in the redshift range $0 < z < 3$, with $6.4 < \log_{10}(M_*/M_\odot) < 12$ and $-4 < \log_{10}(\mathrm{SFR}/M_\odot\,\mathrm{yr}^{-1}) < 3.1$. We then follow the same procedure described in Sect. 2 of Euclid Collaboration: Enia et al. (2024) to produce a realistic catalogue of mock sources that reproduces as closely as possible what is observed in Q1. We perturb the intrinsic fluxes with the noise level found in Q1 in the same set of filters (see Table 1), and cut at observed magnitudes $H_{\rm E} < 24$. Instead of IRAC, in the FS2 simulation these wavelength ranges are covered by mock observations with WISE bands, W1 and W2 (Wright et al. 2010). Given the similar range covered, we ensure that the resulting performance is comparable if not exactly the same.

We then run nnpz with the same reference sample described in Sect. 3, one run with the WISE filters and one without, and produce the recovered results as the median of the 80 NNs. The results are shown in Fig. 2, where we report the recovered versus true relation without (top panel) and with (bottom panel) the two WISE filters. These results follow closely what has already been described in Euclid Collaboration: Enia et al. (2024), at least at the order of magnitude level. It is immediately noticeable how the addition of the two filters at 3.6 µm and 4.5 µm improves parameter estimation, with photo-z NMADs and the outlier fraction decreasing from 0.048 to 0.035 and from 15% to 7%, respectively. The same holds for stellar masses (NMAD decreasing from 0.206 to 0.170 and the outlier fraction from 17% to 12%) and especially for SFRs (NMAD decreasing from 0.643 to 0.446 and the outlier fraction from 25% to 11%). As expected, the recovery of SFMS improves with respect to the case without the two filters in NIR, with a much better recovery of the slope and normalisation of the SFMS relation.

3.3. Photometric redshifts and PPs validation

Quality assessment for the redshifts is performed by looking at how they compare with respect to observed spectroscopic ones. The EDFs cover regions of the sky where there is a plethora of coverage from other spectroscopic surveys. In total, we successfully match 63 504 galaxies with a reliable spectroscopic redshift, that is, with a redshift quality flag of 3 or 4 (see description in Sect. 5.2 of Euclid Collaboration: Tucci et al. 2025). These $z_{\rm spec}$ values are from: the Dark Energy Spectroscopic Instrument (DESI, DESI Collaboration et al. 2016, 2024); the 16th Data Release of the Sloan Digital Sky Survey (SDSS, Ahumada et al. 2020); the 2MASS Redshift Survey (2MRS, Huchra et al. 2012); the PRIsm MUlti-object Survey (PRIMUS, Coil et al. 2011); the Australian Dark Energy Survey (OzDES, Yuan et al. 2015; Childress et al. 2017; Lidman et al. 2020); 3dHST (Brammer et al. 2012); the 2-degree Field Galaxy Redshift Survey (2dFGRS, Colless et al. 2001); the 6-degree Field Galaxy Redshift Survey (6dFGS, Jones et al. 2009); the MOSFIRE Deep Evolution Field Survey (MOSDEF, Kriek et al. 2015); the VANDELS ESO public spectroscopic survey (Pentericci et al. 2018; Talia et al. 2023); the JWST Advanced Deep Extragalactic Survey DR3 (JADES, D'Eugenio et al. 2024); the 2-degree Field Lensing Survey (2dFLens, Blake et al. 2016); and the VIMOS VLT deep survey (VVDS, Le Fèvre et al. 2005).

The results are reported in Fig. 3. In the left panel, we compare the photometric versus spectroscopic redshifts for the subset of reliable spectroscopic redshifts in our sample. These are almost equally divided between EDF-F and EDF-N, with only a handful (123) of objects in EDF-S. The trend we find using *Euclid* real data is similar to what is shown in the previous section, with a non-negligible improvement when adding the two IRAC bands. In particular, compared to the same analysis performed without the addition of the two IRAC bands, the NMAD decreases from 0.06 to 0.04 and the fraction of outliers decreases from 26% to 13%. In the central panels, we plot the normalised difference between spectroscopic and photometric redshifts, as a function of the stellar masses and the SFRs. We do not observe any troubling systematic trend, with the exception of the (expected) behaviour in which galaxies mistakenly placed at higher redshift – mostly those with $(z_{\rm spec} - z_{\rm phot})/(1 + z_{\rm spec}) > -1$ – are found with a wrong higher SFRs, so some caution must be taken when dealing with those high-z galaxies, or with $\log_{10}(\mathrm{SFR}/M_\odot\,\mathrm{yr}^{-1}) > 2.4$.

When looking at the full sample of objects – not just spectroscopic ones – there are no ground-truth values to compare with, but we can still investigate how our results agree with the full distribution of photometric redshifts, stellar masses, and SFRs, especially when compared with other surveys. This is done in the right panels in Fig. 3, where we compare our results for the full sample (in red) with what is observed in COSMOS (in green), at the same magnitude cut applied in this work (i.e., $H_{\rm E} < 24$), and with the same inferred PPs from the Q1 data products (PHZ, in blue). The first two distributions in redshift are comparable, with the main differences observed in a slightly lower fraction of $0.6 < z < 1.2$ objects in our sample (and conversely, a few more $z > 3$ galaxies), while the Q1 data products exhibit a significantly greater number of $z < 0.2$ objects. As for the stellar masses, our results improve with respect to the almost flat at $8 < \log_{10}(M_*/M_\odot) < 9$ distributions of Q1 data products; however, we find relatively fewer objects in the $10.2 < \log_{10}(M_*/M_\odot) < 11.2$ range and conversely more in the $9.2 < \log_{10}(M_*/M_\odot) < 10.2$ range with respect to COSMOS.

In Fig. 4 we report all these information into the M_*–SFR plane, where the SFMS in observed and the main goal of this work. For the subsample of sources with reliable spectroscopic redshift, we plot the median value of the normalized redshift difference in each bin, with red colours highlighting sources mistakenly placed at a higher redshift, and blue colours the opposite. While the latter catastrophic outliers are a small issue only visible in the first redshift interval (with $0.2 < z < 0.5$), the former becomes more and more prominent at higher redshifts (i.e., $z > 1.5$), introducing a non-negligible bias in the estimates of M_* and SFR in the highest mass and SFR regimes, with these skewed towards higher values due to the wrong redshift attribution.

We compare the measured PPs with the ones in the value-added catalogue of PPs in DESI (Siudek et al. 2024), although for a limited number of sources (~ 5 k) in the interval $0 < z < 0.6$. In particular, we confront the SFRs with those obtained from both Hα and Hβ line measurement – not exactly "ground truth" values, but close – while the stellar masses are compared to their SED fitting results. The IMF is the same as the one adopted for this work (Chabrier 2003), and SFRs are obtained from Hα following Kennicutt (1998a). The results are shown in Fig. 5, where the results for each PP is colour-coded as a function of the median value of $(z_{\rm spec} - z_{\rm phot})/(1 + z_{\rm spec})$ in each bin. Despite the limited sample, the performance is in line with what is expected from the simulations. It is immediately clear how the vast majority of catastrophic outliers (i.e., where PPs fall outside of the defined thresholds) are a consequence of sources with a wrong photometric redshift estimate.

Finally, we used these SFRs from Hα and the reliable spectroscopic redshift sample to place some constraints on the estimated uncertainties in the photo-zs and SFRs. Uncertainties are measured from the 16th and 84th percentiles of the weighted distribution of NNs (see Sect. 3). To account for the possibility of an under- (or over-) estimation of those uncertainties, we look at the cumulative distribution of $(z_{\rm phot} - z_{\rm spec})/z_{\rm err}$ – and similarly $({\rm SFR} - {\rm SFR}_{\rm H\alpha})/{\rm SFR}_{\rm err}$ – where we expect 68% of these to fall below 1 if the uncertainties are well-estimated. In contrast, an underestimate would lead to fewer sources within the 1σ limit, and the opposite would be true for an overestimate. These cumulative distributions ("normalized residuals", red for redshifts and blue for SFRs) are reported in Fig. 6. We find that our uncertainties are slightly underestimated for redshifts (1σ level reached for 55% of the sample) and almost spot on for SFRs. We estimate the underestimation of the uncertainties of the photometric redshifts to be a factor of about 1.5.

We take the mode of the distribution of uncertainties as the typical values for each parameter, which are 0.05 for redshifts, 0.11 for stellar masses, and 0.08 for SFRs (on a logarithmic scale). The typical uncertainty on SFRs will be used in the following section for the fit of the SFMS.

4. Results

We start from the sample described in Sect. 2, and limit our analysis to the redshift range between 0.2 and 3.0. This is motivated by the need to obtain a statistically reliable sample in terms of mass completeness and quality of the recovered photometric redshifts and physical properties. In Euclid Collaboration: Enia et al. (2024) it is shown how the main source of biases in the analysis of SFMS during cosmic time – apart from the inherent dispersions in determining the correct PPs – arises from the photo-z estimation, where typically some low-z objects are placed at high-z (up to around 10% of catastrophic outliers) with increased stellar masses and SFRs. The net effect is a steepening of the SFMS at lower redshifts, and the opposite at higher z (see Fig. 11 of Euclid Collaboration: Enia et al. 2024). This is also observed in the validation tests that we performed with simulations and reported in Sect. 3.3 (see Fig. 4).

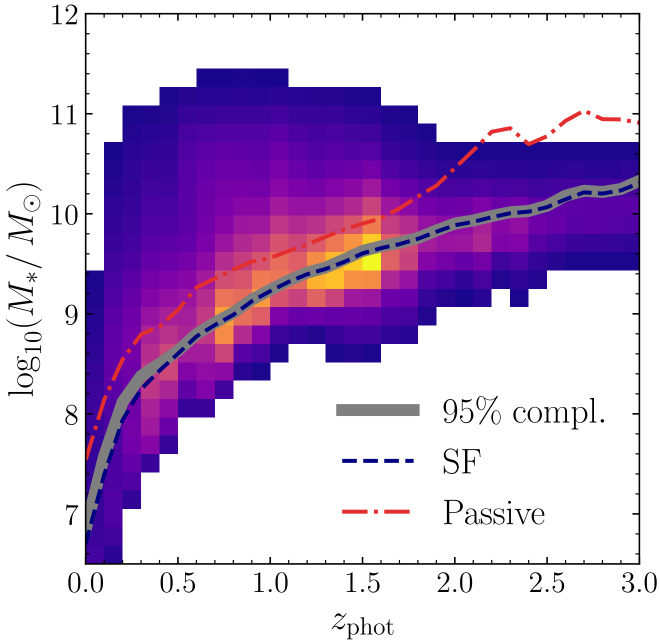

Fig. 7. The stellar mass completeness for the sample used in this work (Pozzetti et al. 2010), with a cut at $H_{\rm E} < 24$, shown as the density of galaxies in the photometric redshifts vs. stellar masses plane. Gray solid line is the 95% stellar mass completeness limit, red dashed-dotted line for passive galaxies, and blue dashed line for SFGs.

We perform our subsequent analysis in the following redshift bins: [0.2, 0.5], [0.5, 0.8], [0.8, 1.5], [1.5, 3.0], with the exception of the morphological analysis, where we stop at $z = 1.5$, since for higher redshifts the quality of the recovered morphological parameters is limited by the sizes of the sources reaching the resolution limit of the survey. Based on the results shown in Fig. 4, we can place a certain degree of confidence in the highest-mass end of the first two redshift intervals, while greater caution is required for the last two. In each case, we limit our analysis – and the reported values – to $\log_{10}(M_*/M_\odot) < 11.5$.

4.1. Mass completeness

We estimate the mass completeness of the sample limited to $H_{\rm E} < 24$ following the method described in Pozzetti et al. (2010). We select galaxies close to the limiting magnitude of our sample, that is, those with $23 < H_{\rm E} < 24$ (with identical results of choosing the faintest 20% as in Pozzetti et al. 2010), and measure for each galaxy

$$\log_{10}(M_{\rm lim}/M_\odot) = \log_{10}(M_*/M_\odot) - 0.4(H_{\rm E} - 24), \qquad (6)$$

representing the mass the galaxies would have at the limiting magnitude. We then measure the 95 percentile of the distribution of $M_{\rm lim}(z)$ for each redshift bin. This is reported in Fig. 7. The classification into star-forming (blue dashed line) and passive galaxies (red dashed-dotted line) is done with the selection criteria based on the NUV–r^+–J diagram (as explained below).

The sample is around 95% complete for M_* that increases from $\log_{10}(M_*/M_\odot) \sim 7$ (at $z \sim 0.1$) to ~ 9 (at $z \sim 1$), and increases from $\log_{10}(M_*/M_\odot) \sim 9.5$ to $\log_{10}(M_*/M_\odot) \sim 10$ while going to higher redshifts, from $z = 1.5$ to 2.5. For passive galaxies, the limit is 0.3 – 0.4 dex higher up to $z \sim 1.8$, and about 0.7 dex higher at $z > 2$.

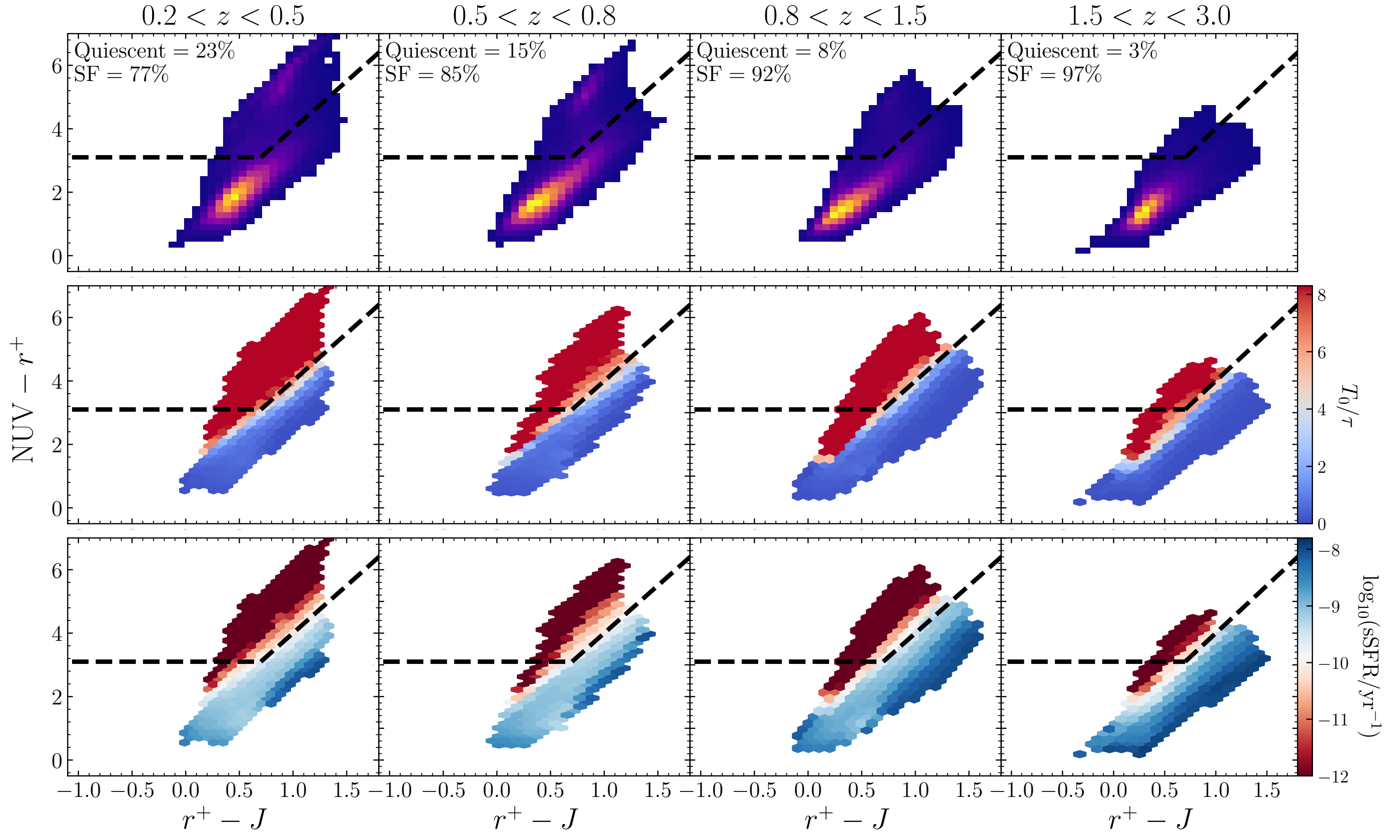

Fig. 8. NUV – r^+ versus $r^+ - J$ rest-frame colours for the sources above the 95% mass completeness limit, in four redshift bins, colour-coded with the density of objects (*upper panels*), the ratio between T_0 and τ (*middle panels*), and the sSFR (*bottom panels*). Dashed-dotted lines divide the regions between star-forming and quiescent galaxies, following the criteria presented in Ilbert et al. (2013).

4.2. Star-forming and passive galaxy classification

Colour-based classifications of galaxies use the principle of separating red and blue galaxies and distinguish between dusty and intrinsically red ones (e.g., the $U-V$ versus $V-J$ colour diagram Labbé et al. 2005; Wuyts et al. 2007; Williams et al. 2010). In this work we use the NUV $-r^+$, r^+-J colours (Ilbert et al. 2010), where star-forming and passive galaxies are discriminated based on their absolute NUV, r^+, and J magnitudes, with quiescent galaxies satisfying the following relations:

$$\mathrm{NUV} - r^+ > 3(r^+ - J) + 1;$$
$$\mathrm{NUV} - r^+ > 3.1. \quad (7)$$

This combination of criteria works in a similar fashion to the UVJ diagram but is more sensitive to recent star-formation via the NUV $- r^+$ colour, which separates passive (redder) and star-forming (bluer) galaxies (Ilbert et al. 2013; Arnouts et al. 2013). Truly passive galaxies are then distinguished from dusty, star-forming objects via the $r^+ - J$ colour, ensuring a proper separation between the two different populations.

The colours NUV $- r^+$ versus $r^+ - J$ of our sample are shown in Fig. 8, colour-coded as a function of the number density of objects with certain colours (top panels) and the median T_0/τ (middle panels) and sSFR in each bin (bottom panels), in the four different redshift bins. Only objects whose mass is higher than the $M_{\mathrm{lim}}(z)$ value at the z_{min} of the redshift bin are shown, to account for sample incompleteness (see Fig. 7). To be consistent with the selection criteria reported above, the adopted absolute magnitude J is not the one estimated in the rest frame *Euclid* J_{E} filter but in the $J_{\mathrm{UltraVISTA}}$ filter (Euclid Collaboration: Schirmer et al. 2022); similarly, we adopt the r^+ band as in Ilbert et al. (2010).

We recover the well-known increase in the fraction of passive galaxies while going to later times, highlighting the assembly of the population of quiescent galaxies observed in the Universe. When checking the colour diagrams against the measured values of sSFR, we notice the presence of a small fraction of objects ($\sim$ 3%) outside the boundaries for quiescent galaxies in the NUV–r^+–J diagram, but with a median value of $\log_{10}(\mathrm{sSFR/yr^{-1}}) < -11$ (and $T_0/\tau > 8$), that is, in a region of the M_*–SFR plane where we would expect only quiescent galaxies. This is a small, negligible number of interlopers, reassuring about the goodness of the classification based on the rest-frame colours.

4.3. The SFR–M_* relation in the EDFs

The M_*–SFR plane for the sample of SFGs selected with the NUV–r^+–J colours is shown in Fig. 9, in four redshift bins, colour-coded in terms of the logarithmic density of objects per bin. The SFMS is observed up to the highest redshift bin ($z < 3$). In the plot, we report three previously published SFMS relations for comparison: Eq. (15) of Popesso et al. (2023, black dashed line), that is, a comprehensive compilation of 27 literature SFMS relations fitted to the same functional form, in the mass range $8.5 < \log_{10}(M_*/M_\odot) < 11.5$; Schreiber et al. (2015, gray dotted line), obtained from $\sim$ 10 k galaxies with the deepest *Herschel* observations of the GOODS and CANDELS-Herschel programme, with $9.5 < \log_{10}(M_*/M_\odot) < 11.5$; Daddi et al. (2022a, blue dashed-dotted line), obtained from a stacking analysis of

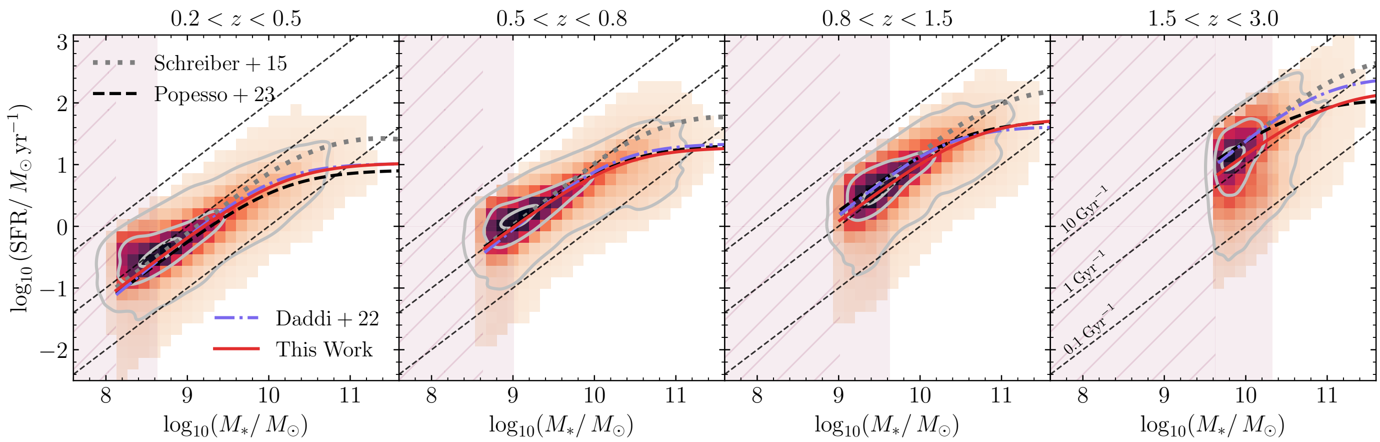

Fig. 9. The SFR–M_* relation for SFGs, selected with the NUV − r^+ versus $r^+ - J$ condition, coloured by the density of objects in each redshift bin. Within the coloured bins there is 99.9% of the sample of SFGs, while the gray contours are the lines enclosing 95%, 50%, and 10% of it. The red line is the fitted SFMS presented in this work, starting from the completeness limit mass at the start of the z-bin. The other SFMSs are from Popesso et al. (2023, dashed black line), Schreiber et al. (2015, dotted gray line), and Daddi et al. (2022a, dashed-dotted blue line), all evaluated at the median redshift of each redshift bin (or to the closest reported value). The purple shaded regions highlights where the mass is below the completeness limit at the start (hatched) and at the end of the redshift bin. Dashed gray lines highlight the region of constant sSFR.

∼ 400 k colour-selected SFGs in COSMOS (Delvecchio et al. 2021), here too in the mass range $8.5 < \log_{10}(M_*/M_\odot) < 11.5$).

All these SFMS forms include the presence of a bending of the relation at the high-mass end. Having enough statistics in terms of the number of objects per bin, we can significantly constrain the deviation from the linear form at high masses. For example, in each redshift interval Delvecchio et al. (2021), Daddi et al. (2022a) found no more than 838 SFGs at $\log_{10}(M_*/M_\odot) > 11$, and in the same mass range the stacking analysis in Schreiber et al. (2015) has < 15 galaxies per bin. Analogously, most of the studies in the compilation of Popesso et al. (2023) stop at $\log_{10}(M_*/M_\odot) = 11$, and those who extend further never reach more than 10^3 galaxies per bin in comparable redshift ranges. Due to the large area observed in Q1, the minimum number of galaxies we have at $\log_{10}(M_*/M_\odot) > 11$ is 875, in the [0.2, 0.5] redshift bin. This number increases to 7640 (for $0.5 < z < 0.8$), 18951 (for $0.8 < z < 1.5$), and 8165 (for $1.5 < z < 3.0$), one or two orders of magnitude higher than the former reported statistics. These numbers are more than enough to subdivide the $\log_{10}(M_*/M_\odot) > 11$ region into two different bins at $z > 0.8$, to better constrain the part of the SFMS where the SFR appears to saturate. The same reasoning, scaled by an order of magnitude, applies if we consider $\log_{10}(M_*/M_\odot) > 10.5$.

Our fit to the observed data is the red line in Fig. 9. Overall, the fits in Popesso et al. (2023) and Daddi et al. (2022a) more resemble our results, while Schreiber et al. (2015) find systematically higher SFRs at the highest mass end. The functional form that we fit these data to, first proposed by Lee et al. (2015), is the same as in Eq. (15) of Popesso et al. (2023) or Eq. (1) of Daddi et al. (2022a)

$$\mathrm{SFR} = \frac{\mathrm{SFR}_{\mathrm{max}}}{1 + (M_0/M_*)^\gamma}, \qquad (8)$$

that is, a parameterisation where the SFR is linked to the stellar mass through three parameters: the bending mass after which the relation deviates from the linear behaviour (M_0); the maximum SFR for $M_* \gg M_0$ ($\mathrm{SFR}_{\mathrm{max}}$); and the slope of the linear relation when $M_* \ll M_0$ (γ). These parameters have been shown to be directly linked to fundamental properties in models of gas accretion (e.g., the bending mass M_0 is directly linked to the ratio between M_{shock} and M_{stream}, see Daddi et al. 2022a,b). For each fit, we keep γ fixed at 1.0, as it has been shown to be a representative value around which almost every fit converges at different redshifts (see Lee et al. 2015; Popesso et al. 2023; Daddi et al. 2022a). This also makes possible a direct comparison with these works in terms of bending mass and maximum SFR.

When fitting the SFMS, we must take into account the fact that for each redshift bin, there are two possible values for the mass completeness limit, depending on whether consider the mass at the lower limit of the redshift bin z_{start} or at the higher limit z_{end}. Depending on the width of the redshift bin, these two masses can differ significantly, of the order of 0.4 – 0.6 dex (see Fig. 9). When $M_* > M_{\mathrm{lim}}(z_{\mathrm{end}})$ we are dealing with a complete sample; in this case, we fit the points measured as the median stellar masses and SFRs of the distribution of SFGs in each bin of mass, with associated uncertainty as the quadrature sum of the standard deviation of the median in each bin and the typical uncertainty on the SFRs (see Sect. 3.3). These are shown as stars in the bottom panel of Fig. 10, coloured as a function of the redshift bin to which they belong. When $M_* < M_{\mathrm{lim}}(z_{\mathrm{start}})$ we consider the sample to be incomplete, and these galaxies are excluded from the fit. In the mass bins where $M_{\mathrm{lim}}(z_{\mathrm{start}}) < M_* < M_{\mathrm{lim}}(z_{\mathrm{end}})$, we are preferentially missing lower-mass galaxies, which tend to have lower SFR. As a result, we treat the SFR data points in these bins as upper limits, as indicated by the arrows in the bottom panel of Fig. 10.

The SFR–mass bins are obtained by binning the distribution of stellar mass to uniformly cover the stellar masses space with a similar number of sources to make these statistically significant. The bins start from where the stellar mass is higher than the 95% completeness limit at the lower limit of the redshift bin, that is, $\log_{10}(M_*/M_\odot) \sim 8.1$ at $z = 0.37$, $\log_{10}(M_*/M_\odot) \sim 8.6$ at $z = 0.67$, $\log_{10}(M_*/M_\odot) \sim 9.0$ at $z = 1.15$ and $\log_{10}(M_*/M_\odot) \sim 9.5$ at $z = 1.83$. The results of the fit are reported in Table 2, and showed in Fig. 10 as dashed lines colour coded by redshift bin. The bending mass and maximum SFR are reported as a function of redshift in the upper panels of Fig. 10, as red stars and solid line. We also show, for comparison, the same parameters found in Daddi et al. (2022a, as blue circles and dashed dotted line) and Popesso et al. (2023, black edged squares and dashed line) as a function of z.

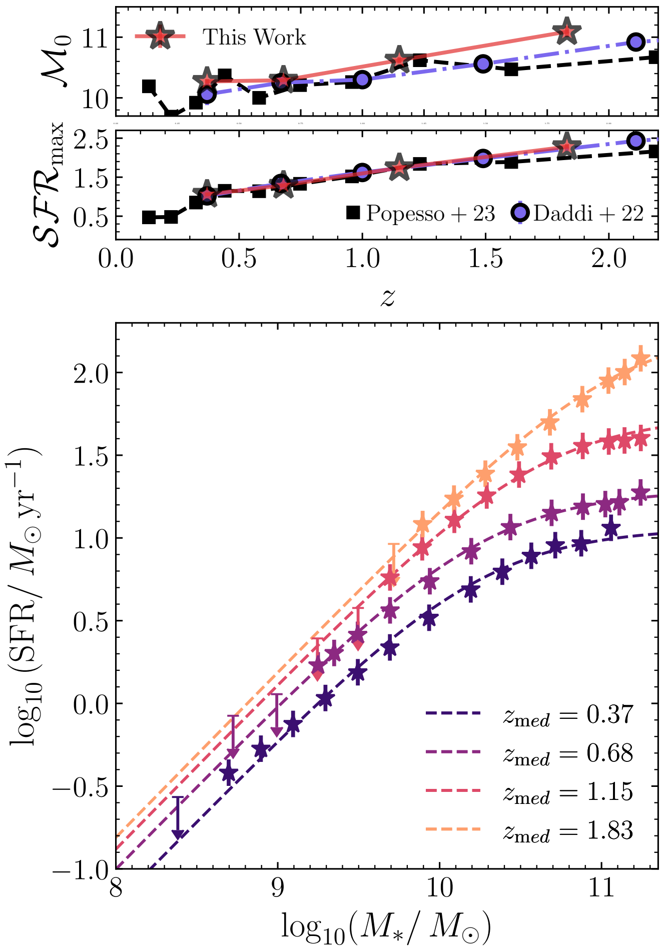

Fig. 10. *Lower panel*: our fit of the SFMS, in the four redshift bins (stars with error bars and arrows) and best-fit model (dashed lines). The reported redshift is the median z of the bin. *Upper panels*: the best-fit (red stars) and reported (squares for Popesso et al. 2023; circles for Daddi et al. 2022a) values for the bending mass and maximum SFR, defined as $\mathcal{M}_0 \equiv \log_{10}(M_0/M_\odot)$ and $\mathcal{SFR}_{\rm max} \equiv \log_{10}(\mathrm{SFR}_{\rm max}/M_\odot\,\mathrm{yr}^{-1})$, as a function of redshift.

Table 2. Fitted values for $\log_{10}(M_0/M_\odot)$, $\log_{10}(\mathrm{SFR}_{\rm max}/M_\odot\,\mathrm{yr}^{-1})$, and the relation scatter $\sigma_{\rm SFMS}$ for each redshift bin, with the median redshift in bin reported in the first column.

$z_{\rm med}$	$\log_{10}(M_0/M_\odot)$	$\log_{10}(\mathrm{SFR}_{\rm max}/M_\odot\,\mathrm{yr}^{-1})$	$\sigma_{\rm SFMS}$
0.37	10.27 ± 0.04	1.06 ± 0.03	0.34 ± 0.11
0.68	10.29 ± 0.05	1.29 ± 0.03	0.27 ± 0.09
1.15	10.62 ± 0.05	1.74 ± 0.04	0.28 ± 0.08
1.83	11.10 ± 0.09	2.28 ± 0.07	0.40 ± 0.12

All bending masses fitted M_0 increase with redshift. We find results similar to those of Daddi et al. (2022a), with the main difference in the [0.8, 1.5] bin, with a higher $\log_{10}(M_0/M_\odot) = 10.62 \pm 0.05$ (similar to what was found in Popesso et al. 2023). In the [1.5, 3.0] bin, our bending mass is more in line with Daddi et al. (2022a) at $\log_{10}(M_0/M_\odot) = 11.10 \pm 0.09$, (0.6 dex higher than the one in Popesso et al. 2023). However, for this redshift bin, we must again warn the reader about the caveats highlighted in Sect. 3.3 and Fig. 4, that is, at $11 < \log_{10}(M_*/M_\odot) < 11.5$ any wrong redshift attribution will introduce an important source of systematic biases, skewing the fitted bins at higher values of M_* and SFR, and therefore the recovered M_0 and $\mathrm{SFR}_{\rm max}$. In any case, the observed agreement and evolution with redshift is remarkable, when taking into account the fact that our SFRs have been evaluated with photometry ranging from the g band (the u band is available only in one field) up to 4.5 µm, thus without properly accounting for dust-obscured star-formation processes, which are disentangled from quiescence only when far-IR and submillimetre photometry is available.

Trying to find the best-fit parameters of the SFMS with the functional form in Eq. (8), we also measure the scatter in the relation $\sigma_{\rm SFMS}$, fitting the difference between the observed set of galaxy stellar masses and SFRs and the model as a normal distribution $\mathcal{N}(\sigma_{\rm SFMS})$. We find the same tight scatter $\sigma_{\rm SFMS} \simeq 0.3$ observed in previous studies, consistent in all redshift intervals within the uncertainties (Table 2).

As an internal check, we also fit the same points with a linear relation (e.g., Eq. 10 in Popesso et al. 2023), obtaining worse χ^2 for each redshift bin with respect to the relation including the bending at the high-mass end.

The SFMS dependence on the absorption A_V and the ratio between the age and the e-folding time τ is shown in the first two rows of Fig. 11, where the colours correspond to the median of A_V and T_0/τ values of the sources within each bin, with the SFMS contours superimposed in gray. In this case, we do not limit the sample to SFGs only (i.e., we do not remove the sources identified as quiescent in the NUV–r^+–J diagram), highlighting a bin when the number of sources within the bin is greater than 20. In this way, we can explore less populated regions of the M_*–SFR plane, where passive galaxies are expected to appear. Of course, the placing in the plane of all the galaxies below a certain limiting sSFR (e.g., 0.01 Gyr^{-1}) should not be considered as absolute, but rather as indicative that those objects are passive galaxies and could lie anywhere below that line. As expected, maximum extinction values ($A_V > 2.0$) are associated with the most massive and star-forming galaxies of the SFMS, with $1 < \mathrm{sSFR/Gyr^{-1}} < 10$, while low or zero dust extinction values are observed at lower sSFRs. Looking at the distribution of fitted A_V, we recover only a small fraction of objects (∼ 1%) with high extinction $A_V > 2.5$, with the A_V distribution peaking at $0.5 < A_V < 1.0$. This could be due to the particular limitations and caveats of the recovered sample (see Sect. 3), especially in the covered range of wavelengths. Lower sSFR galaxies are associated with stellar populations with older ages, in particular at low redshift, and high age/τ ratios, while younger ages are found in the upper part of the SFMS and at high redshift (Nersesian et al. 2025).

The morphological parameters for all the *Euclid* detected sources have been measured by running the `SourceXtractor++` code (Bertin et al. 2020; Kümmel et al. 2022), fitting the detections as two-dimensional Sérsic profiles (see Euclid Collaboration: Romelli et al. 2025 and Euclid Collaboration: Quilley et al. 2025, for further details). Here, we focus on the Sérsic radius R_e and the Sérsic index $n_{\rm S}$. In order to be more conservative, following what was found in Euclid Collaboration: Quilley et al. (2025, see their Fig. 2), in addition to the cuts described in Sect. 2, we also remove the sources whose fit does not converge to a solution. In these cases the Sérsic axis ratio is exactly equal to one, and the Sérsic index $n_{\rm S} < 0.302$ or $n_{\rm S} > 5.45$. These cuts reduce our sample for morphological analysis by 17% leaving a total of 6 702 811 sources.

In the two bottom rows of Fig. 11 we report the SFMS, colour-coded for the median values of $n_{\rm S}$ (middle-bottom row)

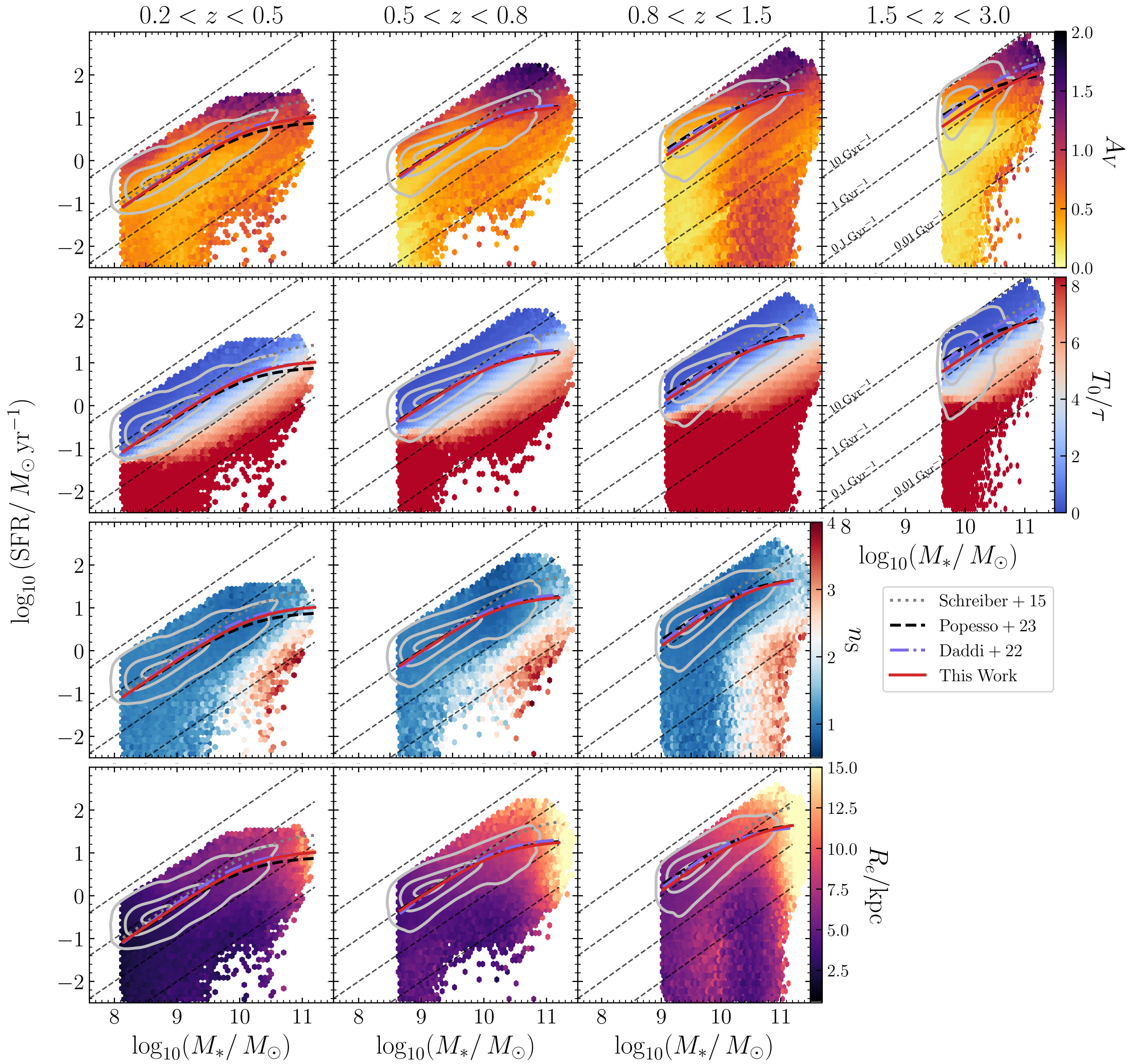

Fig. 11. The SFR–M_* relation, colour-coded by the median A_V (*top*), T_0/τ (*middle-top*), Sérsic index (*middle-bottom*), and Sérsic radius (*bottom*) of objects in each bin. A bin is coloured only when the number of sources falling within the bin is higher than 20. The contours in gray contain 90%, 50%, and 10% of the full sample. The literature SFMS are the same as shown in Fig. 9 and reported in Sect. 4. Dashed lines highlight the loci of equal sSFR.

and R_e (bottom row), converted from arcseconds to kiloparsecs for the predicted photo-z). We note that the higher values of $n_S > 3$ are associated with the most massive, low-sSFR objects, and the radii R_e increase with stellar mass at all redshifts. In all redshift intervals, the concurrent presence of the SFMS and the prominence of exponential disks with $n_S \simeq 1$ (in blue) is immediately visible, while at lower sSFR, close to the limit where measuring SFRs becomes difficult, we note a crowding of sources with de Vaucoulers profiles $n_S \simeq 4$ (in red). Between those, an intermediate region of profiles with $2 < n_S < 3$ (the white strip) at about sSFR $\sim 0.05\,\mathrm{Gyr}^{-1}$, which indicates an evolutionary trend in the structural parameters while moving in the stellar mass–SFR plane, and in total agreement with what has been previously observed in other samples (Wuyts et al. 2011; Martorano et al. 2025). This kind of transition is observed only at the medium-to-high-mass end $\log_{10}(M_*/M_\odot) > 10$, and appears to show only a weak redshift dependence. Interestingly, the mass over which the sequence of passive $n_S \simeq 4$ profiles is observed is almost coincident with the fitted bending mass M_0.

Euclid combines a large sample area with a uniform multiwavelength view, which has great potential for environmental studies. Despite that, here we do not focus on how the environment shapes the SFMS. These effects are difficult to investigate with Q1 data alone, and for some regimes and for a specific population are studied in other Q1 works (Euclid Collaboration: Cleland et al. 2025; Euclid Collaboration: Mai et al. 2025). The soon-to-be-available DR1 observations of the EDFs are expected to have at least ten ROSs, which corresponds to 1.25 magnitude-deeper data. Combining the DR1 data, along with other multi-wavelength observations and the *Euclid* spectroscopy sample, will allow for a thorough investigation of the environmental effects on the SFMS.

5. Conclusions

The *Euclid* Q1 data release, with its first look at the EDFs, is already a good test of the capabilities of the mission to investigate the formation and evolution of galaxies, especially in terms of the enhanced statistics of such a large area of the extragalactic sky. In this work, we have investigated the relation between stellar masses and SFRs, the SFMS, and how it relates to the other well-constrained PPs and morphological parameters, comparing the results with the existing literature, as a fair validation of the *Euclid* results and a first exploration of the mission capabilities to return a statistically robust sample. Even a single ROS of the EDFs is able to yield reliable measurements for the photometric redshifts, stellar masses, and SFRs – which in this work have been improved due to the addition of the first two channels of IRAC – for more than eight million galaxies at a magnitude cut of $H_{\rm E} < 24$. In particular, more than $\sim 30\,$k galaxies are found with $\log_{10}(M_*/M_\odot) > 11$, a substantial improvement over all the other extragalactic surveys limited to a few square degrees of the sky.

The recovered scaling relation between stellar mass and SFR is consistent with what is known from previous studies on the SFMS. The data show a similar tight dispersion (between 0.26 and 0.40 dex), and are in excellent agreement with the functional forms reported in Popesso et al. (2023), Daddi et al. (2022a), and Schreiber et al. (2015). These works fit SFMS with a non-linear term that translates into a bending of the relation, becoming more pronounced at high masses. We fit the relation with the same parameterisation – that is, linking the SFR directly to the bending mass, M_0, and the star-formation rate maximum, $\mathrm{SFR}_{\mathrm{max}}$ – recovering the same statistical agreement with the previous studies. M_0 increases almost monotonically with redshift, starting from $\log_{10}(M_0/M_*) \simeq 10.3$ at $z = 0.37$, up to 11.1 at Cosmic Noon. Our results are in accord with the presence of this reduction in SFR in massive galaxies, with a better χ^2 with respect to a linear one. At the same time, when correlating our results with the catalogue of morphological properties, we recover the well-known bimodality between exponential and smaller star-forming disks and de Vaucoulers profiles for passive and bigger galaxies.

Acknowledgements. AnEn, LuPo, MiBo, EmDa, ViAl, FaGe, SaQu, MaTa, MaSc, and BeGr acknowledge support from the ELSA project. "ELSA: Euclid Legacy Science Advanced analysis tools" (Grant Agreement no. 101135203) is funded by the European Union. Views and opinions expressed are however those of the author(s) only and do not necessarily reflect those of the European Union or Innovate UK. Neither the European Union nor the granting authority can be held responsible for them. UK participation is funded through the UK HORIZON guarantee scheme under Innovate UK grant 10093177. The Euclid Consortium acknowledges the European Space Agency and a number of agencies and institutes that have supported the development of *Euclid*, in particular the Agenzia Spaziale Italiana, the Austrian Forschungsförderungsgesellschaft funded through BMK, the Belgian Science Policy, the Canadian Euclid Consortium, the Deutsches Zentrum für Luft- und Raumfahrt, the DTU Space and the Niels Bohr Institute in Denmark, the French Centre National d'Etudes Spatiales, the Fundação para a Ciência e a Tecnologia, the Hungarian Academy of Sciences, the Ministerio de Ciencia, Innovación y Universidades, the National Aeronautics and Space Administration, the National Astronomical Observatory of Japan, the Netherlandse Onderzoekschool Voor Astronomie, the Norwegian Space Agency, the Research Council of Finland, the Romanian Space Agency, the State Secretariat for Education, Research, and Innovation (SERI) at the Swiss Space Office (SSO), and the United Kingdom Space Agency. A complete and detailed list is available on the *Euclid* web site (www.euclid-ec.org). This work has made use of the *Euclid* Quick Release Q1 data from the *Euclid* mission of the European Space Agency (ESA), 2025, https://doi.org/10.57780/esa-2853f3b. This work has made use of CosmoHub, developed by PIC (maintained by IFAE and CIEMAT) in collaboration with ICE-CSIC. CosmoHub received funding from the Spanish government (MCIN/AEI/10.13039/501100011033), the EU NextGeneration/PRTR (PRTR-C17.I1), and the Generalitat de Catalunya.Based on data from UNIONS, a scientific collaboration using three Hawaii-based telescopes: CFHT, Pan-STARRS, and Subaru www.skysurvey.cc. Based on data from the Dark Energy Camera (DECam) on the Blanco 4-m Telescope at CTIO in Chile https://www.darkenergysurvey.org. In preparation for this work, we used the following codes for Python: Numpy (Harris et al. 2020), Scipy (Virtanen et al. 2020), Pandas (Wes McKinney 2010), nnpz (Tanaka et al. 2018),

References

Abdurro'uf & Akiyama, M. 2017, MNRAS, 469, 2806
Ahumada, R., Allende Prieto, C., Almeida, A., et al. 2020, ApJS, 249, 3
Arnouts, S., Le Floc'h, E., Chevallard, J., et al. 2013, A&A, 558, A67
Baes, M., Nersesian, A., Casasola, V., et al. 2020, A&A, 641, A119
Baker, W. M., Maiolino, R., Bluck, A. F. L., et al. 2022, MNRAS, 510, 3622
Behroozi, P., Wechsler, R. H., Hearin, A. P., & Conroy, C. 2019, MNRAS, 488, 3143
Bertin, E., Schefer, M., Apostolakos, N., et al. 2020, in Astronomical Society of the Pacific Conference Series, Vol. 527, Astronomical Data Analysis Software and Systems XXIX, ed. R. Pizzo, E. R. Deul, J. D. Mol, J. de Plaa, & H. Verkouter, 461
Blake, C., Amon, A., Childress, M., et al. 2016, MNRAS, 462, 4240
Bower, R. G., Schaye, J., Frenk, C. S., et al. 2017, MNRAS, 465, 32
Brammer, G. B., Sánchez-Janssen, R., Labbé, I., et al. 2012, ApJ, 758, L17
Brinchmann, J., Charlot, S., White, S. D. M., et al. 2004, MNRAS, 351, 1151
Bruzual, G. & Charlot, S. 2003, MNRAS, 344, 1000
Calzetti, D., Armus, L., Bohlin, R. C., et al. 2000, ApJ, 533, 682
Chabrier, G. 2003, PASP, 115, 763
Childress, M. J., Lidman, C., Davis, T. M., et al. 2017, MNRAS, 472, 273
Ciesla, L., Elbaz, D., & Fensch, J. 2017, A&A, 608, A41
Clarke, L., Shapley, A. E., Sanders, R. L., et al. 2024, ApJ, 977, 133
Coil, A. L., Blanton, M. R., Burles, S. M., et al. 2011, ApJ, 741, 8
Cole, J. W., Papovich, C., Finkelstein, S. L., et al. 2023, arXiv:2312.10152
Colless, M., Dalton, G., Maddox, S., et al. 2001, MNRAS, 328, 1039
Daddi, E., Delvecchio, I., Dimauro, P., et al. 2022a, A&A, 661, L7
Daddi, E., Dickinson, M., Morrison, G., et al. 2007, ApJ, 670, 156
Daddi, E., Rich, R. M., Valentino, F., et al. 2022b, ApJ, 926, L21
Dark Energy Survey Collaboration, Abbott, T., Abdalla, F. B., et al. 2016, MNRAS, 460, 1270
Dekel, A. & Birnboim, Y. 2006, MNRAS, 368, 2
Delvecchio, I., Daddi, E., Sargent, M. T., et al. 2021, A&A, 647, A123
DESI Collaboration, Adame, A. G., Aguilar, J., et al. 2024, AJ, 168, 58
DESI Collaboration, Aghamousa, A., Aguilar, J., et al. 2016, arXiv:1611.00036
D'Eugenio, F., Cameron, A. J., Scholtz, J., et al. 2024, arXiv:2404.06531
Elbaz, D., Dickinson, M., Hwang, H. S., et al. 2011, A&A, 533, A119
Ellison, S. L., Lin, L., Thorp, M. D., et al. 2021, MNRAS, 501, 4777
Ellison, S. L., Sánchez, S. F., Ibarra-Medel, H., et al. 2018, MNRAS, 474, 2039
Enia, A., Rodighiero, G., Morselli, L., et al. 2020, MNRAS, 493, 4107
Euclid Collaboration: Aussel, H., Tereno, I., Schirmer, M., et al. 2025, A&A, submitted
Euclid Collaboration: Bisigello, L., Rodighiero, G., Fotopoulou, S., et al. 2025, A&A, submitted
Euclid Collaboration: Castander, F., Fosalba, P., Stadel, J., et al. 2024, A&A, accepted, arXiv:2405.13495
Euclid Collaboration: Cleland, C., Mei, S., De Lucia, G., et al. 2025, A&A, submitted
Euclid Collaboration: Corcho-Caballero, P., Ascasibar, Y., Verdoes Kleijn, G., et al. 2025, A&A, submitted
Euclid Collaboration: Cropper, M., Al Bahlawan, A., Amiaux, J., et al. 2024, A&A, accepted, arXiv:2405.13492
Euclid Collaboration: Desprez, G., Paltani, S., Coupon, J., et al. 2020, A&A, 644, A31
Euclid Collaboration: Enia, A., Bolzonella, M., Pozzetti, L., et al. 2024, A&A, 691, A175
Euclid Collaboration: Jahnke, K., Gillard, W., Schirmer, M., et al. 2024, A&A, accepted, arXiv:2405.13493
Euclid Collaboration: Mai, N., Mei, S., Cleland, C., et al. 2025, A&A, submitted
Euclid Collaboration: Matamoro Zatarain, T., Fotopoulou, S., Ricci, F., et al. 2025, A&A, submitted
Euclid Collaboration: McCracken, H., Benson, K., et al. 2025, A&A, submitted

Euclid Collaboration: McPartland, C. J. R., Zalesky, L., Weaver, J. R., et al. 2024, A&A, submitted, arXiv:2408.05275
Euclid Collaboration: Mellier, Y., Abdurro'uf, Acevedo Barroso, J., et al. 2024, A&A, accepted, arXiv:2405.13491
Euclid Collaboration: Moneti, A., McCracken, H. J., Shuntov, M., et al. 2022, A&A, 658, A126
Euclid Collaboration: Polenta, G., Frailis, M., Alavi, A., et al. 2025, A&A, submitted
Euclid Collaboration: Quilley, L., Damjanov, I., de Lapparent, V., et al. 2025, A&A, submitted
Euclid Collaboration: Romelli, E., Kümmel, M., Dole, H., et al. 2025, A&A, submitted
Euclid Collaboration: Scaramella, R., Amiaux, J., Mellier, Y., et al. 2022, A&A, 662, A112
Euclid Collaboration: Schirmer, M., Jahnke, K., Seidel, G., et al. 2022, A&A, 662, A92
Euclid Collaboration: Tucci, M., Paltani, S., Hartley, W., et al. 2025, A&A, submitted
Euclid Collaboration: Walmsley, M., Huertas-Company, M., Quilley, L., et al. 2025, A&A, submitted
Euclid Quick Release Q1. 2025, https://doi.org/10.57780/esa-2853f3b
Fabian, A. C. 2012, ARA&A, 50, 455
Fazio, G. G., Hora, J. L., Allen, L. E., et al. 2004, ApJS, 154, 10
Flaugher, B., Diehl, H. T., Honscheid, K., et al. 2015, AJ, 150, 150
Halton, J. H. 1964, Commun. ACM, 7, 701–702
Harris, C. R., Millman, K. J., van der Walt, S. J., et al. 2020, Nature, 585, 357
Hsieh, B. C., Lin, L., Lin, J. H., et al. 2017, ApJ, 851, L24
Huchra, J. P., Macri, L. M., Masters, K. L., et al. 2012, ApJS, 199, 26
Ilbert, O., McCracken, H. J., Le Fèvre, O., et al. 2013, A&A, 556, A55
Ilbert, O., Salvato, M., Le Floc'h, E., et al. 2010, ApJ, 709, 644
Iyer, K. G., Gawiser, E., Faber, S. M., et al. 2019, ApJ, 879, 116
Jones, D. H., Read, M. A., Saunders, W., et al. 2009, MNRAS, 399, 683
Kennicutt, Robert C., J. 1998a, ApJ, 498, 541
Kennicutt, Jr., R. C. 1998b, ARA&A, 36, 189
Kereš, D., Katz, N., Weinberg, D. H., & Davé, R. 2005, MNRAS, 363, 2
Kriek, M., Shapley, A. E., Reddy, N. A., et al. 2015, ApJS, 218, 15
Kroupa, P. 2001, MNRAS, 322, 231
Kümmel, M., Vassallo, T., Dabin, C., & Gracia Carpio, J. 2022, in Astronomical Society of the Pacific Conference Series, Vol. 532, Astronomical Data Analysis Software and Systems XXX, ed. J. E. Ruiz, F. Pierfedereci, & P. Teuben, 329
Labbé, I., Huang, J., Franx, M., et al. 2005, ApJ, 624, L81
Le Fèvre, O., Vettolani, G., Garilli, B., et al. 2005, A&A, 439, 845
Lee, N., Sanders, D. B., Casey, C. M., et al. 2015, ApJ, 801, 80
Leja, J., Carnall, A. C., Johnson, B. D., Conroy, C., & Speagle, J. S. 2019, ApJ, 876, 3
Leja, J., Speagle, J. S., Ting, Y.-S., et al. 2022, ApJ, 936, 165
Leroy, L., Elbaz, D., Magnelli, B., et al. 2024, A&A, 691, A248
Lidman, C., Tucker, B. E., Davis, T. M., et al. 2020, MNRAS, 496, 19
Lin, L., Belfiore, F., Pan, H.-A., et al. 2017, ApJ, 851, 18
Lin, L., Pan, H.-A., Ellison, S. L., et al. 2019, ApJ, 884, L33
Mancini, C., Daddi, E., Juneau, S., et al. 2019, MNRAS, 489, 1265
Martorano, M., van der Wel, A., Baes, M., et al. 2025, arXiv:2501.02956
Morselli, L., Rodighiero, G., Enia, A., et al. 2020, MNRAS, 496, 4606
Nersesian, A., van der Wel, A., Gallazzi, A. R., et al. 2025, arXiv e-prints, arXiv:2502.03021
Oke, J. B. & Gunn, J. E. 1983, ApJ, 266, 713
Pentericci, L., McLure, R. J., Franzetti, P., Garilli, B., & the VANDELS team. 2018, arXiv:1811.05298
Popesso, P., Concas, A., Cresci, G., et al. 2023, MNRAS, 519, 1526
Popesso, P., Concas, A., Morselli, L., et al. 2019, MNRAS, 483, 3213
Pozzetti, L., Bolzonella, M., Zucca, E., et al. 2010, A&A, 523, A13
Prevot, M. L., Lequeux, J., Maurice, E., Prevot, L., & Rocca-Volmerange, B. 1984, A&A, 132, 389
Rodighiero, G., Daddi, E., Baronchelli, I., et al. 2011, ApJ, 739, L40
Schmidt, M. 1959, ApJ, 129, 243
Schreiber, C., Pannella, M., Elbaz, D., et al. 2015, A&A, 575, A74
Siudek, M., Pucha, R., Mezcua, M., et al. 2024, A&A, 691, A308
Speagle, J. S., Steinhardt, C. L., Capak, P. L., & Silverman, J. D. 2014, ApJS, 214, 15
Talia, M., Schreiber, C., Garilli, B., et al. 2023, A&A, 678, A25
Tanaka, M., Coupon, J., Hsieh, B.-C., et al. 2018, PASJ, 70, S9
Tomczak, A. R., Quadri, R. F., Tran, K.-V. H., et al. 2016, ApJ, 817, 118
Virtanen, P., Gommers, R., Oliphant, T. E., et al. 2020, Nature Methods, 17, 261
Wang, T.-M., Magnelli, B., Schinnerer, E., et al. 2024, A&A, 681, A110
Weaver, J. R., Kauffmann, O. B., Ilbert, O., et al. 2022, ApJS, 258, 11
Werner, M. W., Roellig, T. L., Low, F. J., et al. 2004, ApJS, 154, 1
Wes McKinney. 2010, in Proceedings of the 9th Python in Science Conference, ed. Stéfan van der Walt & Jarrod Millman, 56 – 61
Whitaker, K. E., Franx, M., Leja, J., et al. 2014, ApJ, 795, 104
Williams, R. J., Quadri, R. F., Franx, M., et al. 2010, ApJ, 713, 738
Wright, E. L., Eisenhardt, P. R. M., Mainzer, A. K., et al. 2010, AJ, 140, 1868
Wuyts, S., Förster Schreiber, N. M., Nelson, E. J., et al. 2013, ApJ, 779, 135
Wuyts, S., Förster Schreiber, N. M., van der Wel, A., et al. 2011, ApJ, 742, 96
Wuyts, S., Labbé, I., Franx, M., et al. 2007, ApJ, 655, 51
Yang, X., Mo, H. J., van den Bosch, F. C., et al. 2007, ApJ, 671, 153
Yuan, F., Lidman, C., Davis, T. M., et al. 2015, MNRAS, 452, 3047

[1] Dipartimento di Fisica e Astronomia, Università di Bologna, Via Gobetti 93/2, 40129 Bologna, Italy
[2] INAF-Osservatorio di Astrofisica e Scienza dello Spazio di Bologna, Via Piero Gobetti 93/3, 40129 Bologna, Italy
[3] INAF-Osservatorio Astronomico di Padova, Via dell'Osservatorio 5, 35122 Padova, Italy
[4] Department of Astronomy, University of Geneva, ch. d'Ecogia 16, 1290 Versoix, Switzerland
[5] Max Planck Institute for Extraterrestrial Physics, Giessenbachstr. 1, 85748 Garching, Germany
[6] Universitäts-Sternwarte München, Fakultät für Physik, Ludwig-Maximilians-Universität München, Scheinerstrasse 1, 81679 München, Germany
[7] Université Paris-Saclay, Université Paris Cité, CEA, CNRS, AIM, 91191, Gif-sur-Yvette, France
[8] Instituto de Astrofísica de Canarias (IAC); Departamento de Astrofísica, Universidad de La Laguna (ULL), 38200, La Laguna, Tenerife, Spain
[9] Institute of Space Sciences (ICE, CSIC), Campus UAB, Carrer de Can Magrans, s/n, 08193 Barcelona, Spain
[10] Dipartimento di Fisica e Astronomia "G. Galilei", Università di Padova, Via Marzolo 8, 35131 Padova, Italy
[11] CEA Saclay, DFR/IRFU, Service d'Astrophysique, Bat. 709, 91191 Gif-sur-Yvette, France
[12] SRON Netherlands Institute for Space Research, Landleven 12, 9747 AD, Groningen, The Netherlands
[13] Kapteyn Astronomical Institute, University of Groningen, PO Box 800, 9700 AV Groningen, The Netherlands
[14] INAF-Osservatorio Astronomico di Capodimonte, Via Moiariello 16, 80131 Napoli, Italy
[15] Instituto de Física de Cantabria, Edificio Juan Jordá, Avenida de los Castros, 39005 Santander, Spain
[16] Sterrenkundig Observatorium, Universiteit Gent, Krijgslaan 281 S9, 9000 Gent, Belgium
[17] Johns Hopkins University 3400 North Charles Street Baltimore, MD 21218, USA
[18] STAR Institute, University of Liège, Quartier Agora, Allée du six Août 19c, 4000 Liège, Belgium
[19] INAF-Istituto di Astrofisica e Planetologia Spaziali, via del Fosso del Cavaliere, 100, 00100 Roma, Italy
[20] Leiden Observatory, Leiden University, Einsteinweg 55, 2333 CC Leiden, The Netherlands
[21] Departamento de Física Teórica, Facultad de Ciencias, Universidad Autónoma de Madrid, 28049 Cantoblanco, Madrid, Spain
[22] Centro de Investigación Avanzada en Física Fundamental (CIAFF), Facultad de Ciencias, Universidad Autónoma de Madrid, 28049 Madrid, Spain
[23] Department of Physics and Astronomy, University of British Columbia, Vancouver, BC V6T 1Z1, Canada
[24] Instituto de Astrofísica de Canarias, Vía Láctea, 38205 La Laguna, Tenerife, Spain
[25] Dipartimento di Fisica e Astronomia "Augusto Righi" - Alma Mater Studiorum Università di Bologna, via Piero Gobetti 93/2, 40129 Bologna, Italy
[26] Université Paris-Saclay, CNRS, Institut d'astrophysique spatiale, 91405, Orsay, France
[27] ESAC/ESA, Camino Bajo del Castillo, s/n., Urb. Villafranca del Castillo, 28692 Villanueva de la Cañada, Madrid, Spain
[28] School of Mathematics and Physics, University of Surrey, Guildford, Surrey, GU2 7XH, UK
[29] INAF-Osservatorio Astronomico di Brera, Via Brera 28, 20122 Milano, Italy

[30] IFPU, Institute for Fundamental Physics of the Universe, via Beirut 2, 34151 Trieste, Italy
[31] INAF-Osservatorio Astronomico di Trieste, Via G. B. Tiepolo 11, 34143 Trieste, Italy
[32] INFN, Sezione di Trieste, Via Valerio 2, 34127 Trieste TS, Italy
[33] SISSA, International School for Advanced Studies, Via Bonomea 265, 34136 Trieste TS, Italy
[34] INFN-Sezione di Bologna, Viale Berti Pichat 6/2, 40127 Bologna, Italy
[35] Centre National d'Etudes Spatiales – Centre spatial de Toulouse, 18 avenue Edouard Belin, 31401 Toulouse Cedex 9, France
[36] Space Science Data Center, Italian Space Agency, via del Politecnico snc, 00133 Roma, Italy
[37] Dipartimento di Fisica, Università di Genova, Via Dodecaneso 33, 16146, Genova, Italy
[38] INFN-Sezione di Genova, Via Dodecaneso 33, 16146, Genova, Italy
[39] Department of Physics "E. Pancini", University Federico II, Via Cinthia 6, 80126, Napoli, Italy
[40] Instituto de Astrofísica e Ciências do Espaço, Universidade do Porto, CAUP, Rua das Estrelas, PT4150-762 Porto, Portugal
[41] Faculdade de Ciências da Universidade do Porto, Rua do Campo de Alegre, 4150-007 Porto, Portugal
[42] Dipartimento di Fisica, Università degli Studi di Torino, Via P. Giuria 1, 10125 Torino, Italy
[43] INFN-Sezione di Torino, Via P. Giuria 1, 10125 Torino, Italy
[44] INAF-Osservatorio Astrofisico di Torino, Via Osservatorio 20, 10025 Pino Torinese (TO), Italy
[45] European Space Agency/ESTEC, Keplerlaan 1, 2201 AZ Noordwijk, The Netherlands
[46] Institute Lorentz, Leiden University, Niels Bohrweg 2, 2333 CA Leiden, The Netherlands
[47] INAF-IASF Milano, Via Alfonso Corti 12, 20133 Milano, Italy
[48] Centro de Investigaciones Energéticas, Medioambientales y Tecnológicas (CIEMAT), Avenida Complutense 40, 28040 Madrid, Spain
[49] Port d'Informació Científica, Campus UAB, C. Albareda s/n, 08193 Bellaterra (Barcelona), Spain
[50] Institute for Theoretical Particle Physics and Cosmology (TTK), RWTH Aachen University, 52056 Aachen, Germany
[51] Institut d'Estudis Espacials de Catalunya (IEEC), Edifici RDIT, Campus UPC, 08860 Castelldefels, Barcelona, Spain
[52] INAF-Osservatorio Astronomico di Roma, Via Frascati 33, 00078 Monteporzio Catone, Italy
[53] INFN section of Naples, Via Cinthia 6, 80126, Napoli, Italy
[54] Institute for Astronomy, University of Hawaii, 2680 Woodlawn Drive, Honolulu, HI 96822, USA
[55] Dipartimento di Fisica e Astronomia "Augusto Righi" - Alma Mater Studiorum Università di Bologna, Viale Berti Pichat 6/2, 40127 Bologna, Italy
[56] Institute for Astronomy, University of Edinburgh, Royal Observatory, Blackford Hill, Edinburgh EH9 3HJ, UK
[57] Jodrell Bank Centre for Astrophysics, Department of Physics and Astronomy, University of Manchester, Oxford Road, Manchester M13 9PL, UK
[58] European Space Agency/ESRIN, Largo Galileo Galilei 1, 00044 Frascati, Roma, Italy
[59] Université Claude Bernard Lyon 1, CNRS/IN2P3, IP2I Lyon, UMR 5822, Villeurbanne, F-69100, France
[60] Institut de Ciències del Cosmos (ICCUB), Universitat de Barcelona (IEEC-UB), Martí i Franquès 1, 08028 Barcelona, Spain
[61] Institució Catalana de Recerca i Estudis Avançats (ICREA), Passeig de Lluís Companys 23, 08010 Barcelona, Spain
[62] UCB Lyon 1, CNRS/IN2P3, IUF, IP2I Lyon, 4 rue Enrico Fermi, 69622 Villeurbanne, France
[63] Mullard Space Science Laboratory, University College London, Holmbury St Mary, Dorking, Surrey RH5 6NT, UK
[64] Departamento de Física, Faculdade de Ciências, Universidade de Lisboa, Edifício C8, Campo Grande, PT1749-016 Lisboa, Portugal
[65] Instituto de Astrofísica e Ciências do Espaço, Faculdade de Ciências, Universidade de Lisboa, Campo Grande, 1749-016 Lisboa, Portugal
[66] INFN-Padova, Via Marzolo 8, 35131 Padova, Italy
[67] Aix-Marseille Université, CNRS/IN2P3, CPPM, Marseille, France
[68] INFN-Bologna, Via Irnerio 46, 40126 Bologna, Italy
[69] School of Physics, HH Wills Physics Laboratory, University of Bristol, Tyndall Avenue, Bristol, BS8 1TL, UK
[70] FRACTAL S.L.N.E., calle Tulipán 2, Portal 13 1A, 28231, Las Rozas de Madrid, Spain
[71] Dipartimento di Fisica "Aldo Pontremoli", Università degli Studi di Milano, Via Celoria 16, 20133 Milano, Italy
[72] INFN-Sezione di Milano, Via Celoria 16, 20133 Milano, Italy
[73] NRC Herzberg, 5071 West Saanich Rd, Victoria, BC V9E 2E7, Canada
[74] Institute of Theoretical Astrophysics, University of Oslo, P.O. Box 1029 Blindern, 0315 Oslo, Norway
[75] Jet Propulsion Laboratory, California Institute of Technology, 4800 Oak Grove Drive, Pasadena, CA, 91109, USA
[76] Department of Physics, Lancaster University, Lancaster, LA1 4YB, UK
[77] Felix Hormuth Engineering, Goethestr. 17, 69181 Leimen, Germany
[78] Technical University of Denmark, Elektrovej 327, 2800 Kgs. Lyngby, Denmark
[79] Cosmic Dawn Center (DAWN), Denmark
[80] Institut d'Astrophysique de Paris, UMR 7095, CNRS, and Sorbonne Université, 98 bis boulevard Arago, 75014 Paris, France
[81] Max-Planck-Institut für Astronomie, Königstuhl 17, 69117 Heidelberg, Germany
[82] NASA Goddard Space Flight Center, Greenbelt, MD 20771, USA
[83] Department of Physics and Astronomy, University College London, Gower Street, London WC1E 6BT, UK
[84] Department of Physics and Helsinki Institute of Physics, Gustaf Hällströmin katu 2, 00014 University of Helsinki, Finland
[85] Université de Genève, Département de Physique Théorique and Centre for Astroparticle Physics, 24 quai Ernest-Ansermet, CH-1211 Genève 4, Switzerland
[86] Department of Physics, P.O. Box 64, 00014 University of Helsinki, Finland
[87] Helsinki Institute of Physics, Gustaf Hällströmin katu 2, University of Helsinki, Helsinki, Finland
[88] Centre de Calcul de l'IN2P3/CNRS, 21 avenue Pierre de Coubertin 69627 Villeurbanne Cedex, France
[89] Laboratoire d'etude de l'Univers et des phenomenes eXtremes, Observatoire de Paris, Université PSL, Sorbonne Université, CNRS, 92190 Meudon, France
[90] Aix-Marseille Université, CNRS, CNES, LAM, Marseille, France
[91] SKA Observatory, Jodrell Bank, Lower Withington, Macclesfield, Cheshire SK11 9FT, UK
[92] Universität Bonn, Argelander-Institut für Astronomie, Auf dem Hügel 71, 53121 Bonn, Germany
[93] INFN-Sezione di Roma, Piazzale Aldo Moro, 2 - c/o Dipartimento di Fisica, Edificio G. Marconi, 00185 Roma, Italy
[94] Department of Physics, Institute for Computational Cosmology, Durham University, South Road, Durham, DH1 3LE, UK
[95] Infrared Processing and Analysis Center, California Institute of Technology, Pasadena, CA 91125, USA
[96] Université Côte d'Azur, Observatoire de la Côte d'Azur, CNRS, Laboratoire Lagrange, Bd de l'Observatoire, CS 34229, 06304 Nice cedex 4, France
[97] Université Paris Cité, CNRS, Astroparticule et Cosmologie, 75013 Paris, France
[98] CNRS-UCB International Research Laboratory, Centre Pierre Binetruy, IRL2007, CPB-IN2P3, Berkeley, USA
[99] University of Applied Sciences and Arts of Northwestern Switzerland, School of Engineering, 5210 Windisch, Switzerland
[100] Institut d'Astrophysique de Paris, 98bis Boulevard Arago, 75014, Paris, France

[101] Institute of Physics, Laboratory of Astrophysics, Ecole Polytechnique Fédérale de Lausanne (EPFL), Observatoire de Sauverny, 1290 Versoix, Switzerland
[102] Aurora Technology for European Space Agency (ESA), Camino bajo del Castillo, s/n, Urbanizacion Villafranca del Castillo, Villanueva de la Cañada, 28692 Madrid, Spain
[103] Institut de Física d'Altes Energies (IFAE), The Barcelona Institute of Science and Technology, Campus UAB, 08193 Bellaterra (Barcelona), Spain
[104] School of Mathematics, Statistics and Physics, Newcastle University, Herschel Building, Newcastle-upon-Tyne, NE1 7RU, UK
[105] DARK, Niels Bohr Institute, University of Copenhagen, Jagtvej 155, 2200 Copenhagen, Denmark
[106] Waterloo Centre for Astrophysics, University of Waterloo, Waterloo, Ontario N2L 3G1, Canada
[107] Department of Physics and Astronomy, University of Waterloo, Waterloo, Ontario N2L 3G1, Canada
[108] Perimeter Institute for Theoretical Physics, Waterloo, Ontario N2L 2Y5, Canada
[109] Institute of Space Science, Str. Atomistilor, nr. 409 Măgurele, Ilfov, 077125, Romania
[110] Consejo Superior de Investigaciones Cientificas, Calle Serrano 117, 28006 Madrid, Spain
[111] Universidad de La Laguna, Departamento de Astrofísica, 38206 La Laguna, Tenerife, Spain
[112] Caltech/IPAC, 1200 E. California Blvd., Pasadena, CA 91125, USA
[113] Institut für Theoretische Physik, University of Heidelberg, Philosophenweg 16, 69120 Heidelberg, Germany
[114] Institut de Recherche en Astrophysique et Planétologie (IRAP), Université de Toulouse, CNRS, UPS, CNES, 14 Av. Edouard Belin, 31400 Toulouse, France
[115] Université St Joseph; Faculty of Sciences, Beirut, Lebanon
[116] Departamento de Física, FCFM, Universidad de Chile, Blanco Encalada 2008, Santiago, Chile
[117] Universität Innsbruck, Institut für Astro- und Teilchenphysik, Technikerstr. 25/8, 6020 Innsbruck, Austria
[118] Satlantis, University Science Park, Sede Bld 48940, Leioa-Bilbao, Spain
[119] Centre for Electronic Imaging, Open University, Walton Hall, Milton Keynes, MK7 6AA, UK
[120] Instituto de Astrofísica e Ciências do Espaço, Faculdade de Ciências, Universidade de Lisboa, Tapada da Ajuda, 1349-018 Lisboa, Portugal
[121] Cosmic Dawn Center (DAWN)
[122] Niels Bohr Institute, University of Copenhagen, Jagtvej 128, 2200 Copenhagen, Denmark
[123] Universidad Politécnica de Cartagena, Departamento de Electrónica y Tecnología de Computadoras, Plaza del Hospital 1, 30202 Cartagena, Spain
[124] Dipartimento di Fisica e Scienze della Terra, Università degli Studi di Ferrara, Via Giuseppe Saragat 1, 44122 Ferrara, Italy
[125] Istituto Nazionale di Fisica Nucleare, Sezione di Ferrara, Via Giuseppe Saragat 1, 44122 Ferrara, Italy
[126] INAF, Istituto di Radioastronomia, Via Piero Gobetti 101, 40129 Bologna, Italy
[127] Department of Physics, Oxford University, Keble Road, Oxford OX1 3RH, UK
[128] Université PSL, Observatoire de Paris, Sorbonne Université, CNRS, LERMA, 75014, Paris, France
[129] Université Paris-Cité, 5 Rue Thomas Mann, 75013, Paris, France
[130] INAF-Osservatorio Astronomico di Brera, Via Brera 28, 20122 Milano, Italy, and INFN-Sezione di Genova, Via Dodecaneso 33, 16146, Genova, Italy
[131] ICL, Junia, Université Catholique de Lille, LITL, 59000 Lille, France
[132] ICSC - Centro Nazionale di Ricerca in High Performance Computing, Big Data e Quantum Computing, Via Magnanelli 2, Bologna, Italy
[133] Instituto de Física Teórica UAM-CSIC, Campus de Cantoblanco, 28049 Madrid, Spain
[134] CERCA/ISO, Department of Physics, Case Western Reserve University, 10900 Euclid Avenue, Cleveland, OH 44106, USA
[135] Technical University of Munich, TUM School of Natural Sciences, Physics Department, James-Franck-Str. 1, 85748 Garching, Germany
[136] Max-Planck-Institut für Astrophysik, Karl-Schwarzschild-Str. 1, 85748 Garching, Germany
[137] Laboratoire Univers et Théorie, Observatoire de Paris, Université PSL, Université Paris Cité, CNRS, 92190 Meudon, France
[138] Departamento de Física Fundamental. Universidad de Salamanca. Plaza de la Merced s/n. 37008 Salamanca, Spain
[139] Université de Strasbourg, CNRS, Observatoire astronomique de Strasbourg, UMR 7550, 67000 Strasbourg, France
[140] Center for Data-Driven Discovery, Kavli IPMU (WPI), UTIAS, The University of Tokyo, Kashiwa, Chiba 277-8583, Japan
[141] Ludwig-Maximilians-University, Schellingstrasse 4, 80799 Munich, Germany
[142] Max-Planck-Institut für Physik, Boltzmannstr. 8, 85748 Garching, Germany
[143] Dipartimento di Fisica - Sezione di Astronomia, Università di Trieste, Via Tiepolo 11, 34131 Trieste, Italy
[144] NASA Ames Research Center, Moffett Field, CA 94035, USA
[145] Bay Area Environmental Research Institute, Moffett Field, California 94035, USA
[146] California Institute of Technology, 1200 E California Blvd, Pasadena, CA 91125, USA
[147] Department of Physics & Astronomy, University of California Irvine, Irvine CA 92697, USA
[148] Department of Mathematics and Physics E. De Giorgi, University of Salento, Via per Arnesano, CP-I93, 73100, Lecce, Italy
[149] INFN, Sezione di Lecce, Via per Arnesano, CP-193, 73100, Lecce, Italy
[150] INAF-Sezione di Lecce, c/o Dipartimento Matematica e Fisica, Via per Arnesano, 73100, Lecce, Italy
[151] Departamento Física Aplicada, Universidad Politécnica de Cartagena, Campus Muralla del Mar, 30202 Cartagena, Murcia, Spain
[152] Institute of Cosmology and Gravitation, University of Portsmouth, Portsmouth PO1 3FX, UK
[153] Department of Computer Science, Aalto University, PO Box 15400, Espoo, FI-00 076, Finland
[154] Instituto de Astrofísica de Canarias, c/ Via Lactea s/n, La Laguna 38200, Spain. Departamento de Astrofísica de la Universidad de La Laguna, Avda. Francisco Sanchez, La Laguna, 38200, Spain
[155] Ruhr University Bochum, Faculty of Physics and Astronomy, Astronomical Institute (AIRUB), German Centre for Cosmological Lensing (GCCL), 44780 Bochum, Germany
[156] Department of Physics and Astronomy, Vesilinnantie 5, 20014 University of Turku, Finland
[157] Serco for European Space Agency (ESA), Camino bajo del Castillo, s/n, Urbanizacion Villafranca del Castillo, Villanueva de la Cañada, 28692 Madrid, Spain
[158] ARC Centre of Excellence for Dark Matter Particle Physics, Melbourne, Australia
[159] Centre for Astrophysics & Supercomputing, Swinburne University of Technology, Hawthorn, Victoria 3122, Australia
[160] Department of Physics and Astronomy, University of the Western Cape, Bellville, Cape Town, 7535, South Africa
[161] DAMTP, Centre for Mathematical Sciences, Wilberforce Road, Cambridge CB3 0WA, UK
[162] Kavli Institute for Cosmology Cambridge, Madingley Road, Cambridge, CB3 0HA, UK
[163] Department of Astrophysics, University of Zurich, Winterthurerstrasse 190, 8057 Zurich, Switzerland
[164] Department of Physics, Centre for Extragalactic Astronomy, Durham University, South Road, Durham, DH1 3LE, UK
[165] IRFU, CEA, Université Paris-Saclay 91191 Gif-sur-Yvette Cedex, France

[166] Oskar Klein Centre for Cosmoparticle Physics, Department of Physics, Stockholm University, Stockholm, SE-106 91, Sweden
[167] Astrophysics Group, Blackett Laboratory, Imperial College London, London SW7 2AZ, UK
[168] Univ. Grenoble Alpes, CNRS, Grenoble INP, LPSC-IN2P3, 53, Avenue des Martyrs, 38000, Grenoble, France
[169] INAF-Osservatorio Astrofisico di Arcetri, Largo E. Fermi 5, 50125, Firenze, Italy
[170] Dipartimento di Fisica, Sapienza Università di Roma, Piazzale Aldo Moro 2, 00185 Roma, Italy
[171] Centro de Astrofísica da Universidade do Porto, Rua das Estrelas, 4150-762 Porto, Portugal
[172] HE Space for European Space Agency (ESA), Camino bajo del Castillo, s/n, Urbanizacion Villafranca del Castillo, Villanueva de la Cañada, 28692 Madrid, Spain
[173] Department of Astrophysical Sciences, Peyton Hall, Princeton University, Princeton, NJ 08544, USA
[174] Theoretical astrophysics, Department of Physics and Astronomy, Uppsala University, Box 515, 751 20 Uppsala, Sweden
[175] Minnesota Institute for Astrophysics, University of Minnesota, 116 Church St SE, Minneapolis, MN 55455, USA
[176] Mathematical Institute, University of Leiden, Einsteinweg 55, 2333 CA Leiden, The Netherlands
[177] School of Physics & Astronomy, University of Southampton, Highfield Campus, Southampton SO17 1BJ, UK
[178] Institute of Astronomy, University of Cambridge, Madingley Road, Cambridge CB3 0HA, UK
[179] Department of Physics and Astronomy, University of California, Davis, CA 95616, USA
[180] Space physics and astronomy research unit, University of Oulu, Pentti Kaiteran katu 1, FI-90014 Oulu, Finland
[181] Center for Computational Astrophysics, Flatiron Institute, 162 5th Avenue, 10010, New York, NY, USA